

# **Nanotools for Combined AFM-SECM Experiments in Structural Biology**

**Thèse présentée à la Faculté des Sciences**

**Institut de Microtechnique**

**Université de Neuchâtel**

**Pour l'obtention du grade de docteur ès sciences**

**par**

**Rosario Maurizio Gullo**

**Acceptée sur proposition du jury:**

**Mme. M. Koudelka-Hep**

**MM. U. Staufer (directeur de thèse)**

**N. de Rooij**

**A. Engel (Bâle)**

**H. Siegenthaler (Berne)**

**Soutenue le 24 août 2006**

**Université de Neuchâtel**

**2007**





## IMPRIMATUR POUR LA THESE

# Nanotools for combined AFM-SECM experiments in structural biology

## Rosario Maurizio GULLO

---

UNIVERSITE DE NEUCHÂTEL

FACULTE DES SCIENCES

La Faculté des sciences de l'Université de Neuchâtel,  
sur le rapport des membres du jury

Mme M. Koudelka-Hep,  
MM. U. Staufer (directeur de thèse),  
N. de Rooij, A. Engel (Bâle)  
et H. Siegenthaler (Berne)

autorise l'impression de la présente thèse.

Neuchâtel, le 13 octobre 2006

UNIVERSITE DE NEUCHÂTEL  
FACULTE DES SCIENCES  
Secrétariat-décanat de la faculté  
Rue Emile-Argand 11 - CP 158  
CH-2009 Neuchâtel  
*M. Couvry*

J.-P. Derendinger



*"Kachi wa saya no naka ni ari"*



# Abstract

Keywords in french: Microscopie à force atomique, microscopie électrochimique à balayage, canaux ioniques, biologie cellulaire, micro fluidique.

Keywords in english: Atomic force microscopy, scanning electrochemical microscopy, ion channels, cell biology, micro fluidic.

Many important biological activities like electrical impulses in nerve cells and cell metabolism are strongly related to the transport of molecules into and out of biological cells. Consequently, there is great interest in understanding these cellular transport mechanisms. The patch clamp technique gives a quantitative insight in cellular transport. This method generally uses a glass pipette to measure the electrochemical current across the cell membrane. Atomic force microscopy (AFM), on the other hand, has been applied to study the topography of membranes. To get a quantitative and qualitative comprehension of the cellular transport it would be advantageous to observe the topographic and local electrical information simultaneously. This could be achieved by a setup that combines the conventional patch clamp technique and AFM. However, the combination and implementation of these two techniques requires the contrivance of new tools. This thesis is devoted to the fabrication and characterization of such tools. In a first step the glass pipette used in patch clamp has been replaced by a planar sample support, which is more adapted to the requirements of AFM. The supports feature a nanometer scaled aperture in order to enable measurements on suspended membrane patches. Their electrical, mechanical and biological characteristics were investigated and designed to fit the requirements of the aimed

application. In order to keep the biological cells functional, the experiments need to be performed in a liquid environment. Therefore a special conductive AFM probe allowing local electrical measurements in liquid environment has been designed and realized. The probe is electrically insulated except at the very apex of the tip, which has a radius of curvature smaller than 10nm. The imaging quality of the probe has been assessed and nanometer lateral resolution on biological membranes has been achieved. The electrochemical behavior of the tip has been investigated by cyclic voltammetry. Moreover the probes were employed to perform combined AFM and scanning electrochemical microscopy (SECM) experiments. It was possible to simultaneously acquire the topography and the electrochemical current images with a lateral resolution below 10nm. Measurements through the submicron scaled aperture in the planar sample support were used to investigate the distance dependency of the electrochemical current. First measurements on biological cells absorbed on the planar sample support showed an excellent correlation between topography and electrochemical current. In order to gain a deeper insight into the relation between the tip geometry and the resulting electrochemical current and imaging resolution, a finite element simulation model has been built. The simulations agreed with the measurements and theory. This results proved the accuracy of the finite element model.

# Contents

<b>Abstract</b>	<b>i</b>
<b>I Introduction</b>	<b>1</b>
<b>1 Theory</b>	<b>3</b>
1.1 Cell Biology . . . . .	3
1.1.1 Cellular Transport . . . . .	4
1.2 Patch Clamp . . . . .	7
1.2.1 Electrical Potentials and Currents in Cells . . . . .	8
1.2.2 Electrodes . . . . .	8
1.2.3 Capacitors in Cells . . . . .	9
1.2.4 Current Clamp and Voltage Clamp . . . . .	11
1.2.5 Glass Microelectrodes and Tight Seals . . . . .	12
1.3 Combining AFM and Patch Clamp . . . . .	13
1.4 Scanning Electrochemical Microscopy . . . . .	15
1.4.1 Instrumentation . . . . .	16
1.4.2 Electrodes . . . . .	16
1.4.3 SECM Imaging . . . . .	17
1.4.4 Surface Modification by SECM . . . . .	22
1.4.5 SECM Applications . . . . .	22
Bibliography . . . . .	24

---

<b>II</b>	<b>Implementation and Experiments</b>	<b>35</b>
<b>2</b>	<b>Fabrication</b>	<b>39</b>
2.1	Towards a Planar Sample Support for in situ Experiments in Structural Biology . . . . .	40
2.1.1	Introduction . . . . .	40
2.1.2	Fabrication . . . . .	41
2.1.3	Experiments . . . . .	42
2.1.4	Conclusion . . . . .	45
	Bibliography . . . . .	46
2.2	Latest Results for the Sample Support . . . . .	48
	Bibliography . . . . .	51
2.3	Insulated Conductive Probes for in-situ Experiments in Cell Biology . . . . .	52
2.3.1	Introduction . . . . .	52
2.3.2	Probe Design . . . . .	53
2.3.3	Fabrication . . . . .	55
2.3.4	Experiments . . . . .	56
2.3.5	Conclusion . . . . .	57
	Bibliography . . . . .	58
<b>3</b>	<b>Experiments</b>	<b>59</b>
3.1	Microfabricated Probes for Combined Atomic Force and Scanning Electrochemical Microscopy . . . . .	60
3.1.1	Introduction . . . . .	60
3.1.2	Experimental Setup and Finite Element Model . . . . .	61
3.1.3	Experimental and Simulation Results . . . . .	67
3.1.4	Conclusion . . . . .	77
	Bibliography . . . . .	78
3.2	Latest Results . . . . .	83
3.2.1	First Combined AFM-SECM Experiments on the Planar Sample Support and Biological Cells . . . . .	83
3.2.2	Venturi Effect with the Planar Sample Support . . . . .	85



<b>4</b>	<b>Summary, Conclusion and Outlook</b>	<b>89</b>
4.1	Planar Sample Support Fabrication . . . . .	89
4.2	Experiments . . . . .	90
4.3	Outlook . . . . .	91
<b>III</b>	<b>Appendix</b>	<b>93</b>
<b>A</b>	<b>Planar Sample Support Process Flow</b>	<b>95</b>
<b>B</b>	<b>Conductive Probe Process Flow</b>	<b>101</b>
<b>IV</b>	<b>Addendum</b>	<b>107</b>
	<b>Acknowledgements</b>	<b>109</b>
	<b>Publications</b>	<b>111</b>
B.1	Papers . . . . .	112
B.2	Proceedings . . . . .	113
B.2.1	Academic Year: 2004 – 2005 . . . . .	113
B.2.2	Academic Year: 2003 – 2004 . . . . .	113
B.2.3	Academic Year: 2002 – 2003 . . . . .	114



# List of Figures

1.1	A Model of a Cell Membrane . . . . .	4
1.2	Passive Membrane Transport . . . . .	6
1.3	Sodium-Potassium ATPase Pump . . . . .	6
1.4	Electrical Model of the Cell Membrane . . . . .	10
1.5	Effect of the Capacitance . . . . .	10
1.6	Patch Clamp Micro Pipette . . . . .	11
1.7	Patch Clamp Configurations . . . . .	12
1.8	Leakage Current in Patch Clamp . . . . .	13
1.9	AFM - Patch Clamp Setup . . . . .	15
1.10	SECM Setup . . . . .	16
1.11	SEM Micrographs of a UME . . . . .	18
1.12	Cyclic Voltammogram . . . . .	19
1.13	Electrochemical Approach Curves . . . . .	20
1.14	SECM Micrograph . . . . .	21
1.15	G/C Mode and Surface Modification by SECM . . . . .	22
2.1	Schematic Representation of the Setup . . . . .	41
2.2	Surface Roughness . . . . .	43
2.3	SEM Pictures of the Patch Site . . . . .	44
2.4	Resistance of the Hole . . . . .	45
2.5	Phase Gain Plot of the Planar Support Chip . . . . .	48
2.6	Resistance of the 100nm Aperture . . . . .	49
2.7	Capacitance of the New Planar Sample Support . . . . .	50
2.8	Experimental Setup . . . . .	53

---

2.9	Schematic Representation of the AFM Probe . . . . .	54
2.10	Sem Pictures of the Fabricated Probes . . . . .	54
2.11	Approach Curves on HOPG . . . . .	55
2.12	AFM Topography Micrograph . . . . .	56
2.13	Topography and Current on HOPG . . . . .	56
3.1	Schematic Representation of the Conductive Probe and TEM Micrographs . . . . .	62
3.2	Schematic Representation of the Monopotentiostat Setup . .	64
3.3	Diagram of a Conical Electrode . . . . .	65
3.4	Cyclic Voltammograms 1 . . . . .	68
3.5	Cyclic Voltammograms 2 . . . . .	69
3.6	Simulated Concentration Gradients . . . . .	71
3.7	AFM-SECM Approach Curves . . . . .	72
3.8	AFM-SECM Approach Curves and Simulations . . . . .	73
3.9	Simulated Concentration Gradients for Different Distances .	74
3.10	AFM-SECM Images . . . . .	76
3.11	AFM-SECM on Planar Sample Support . . . . .	84
3.12	BHK Cells on the Planar Sample Support . . . . .	85
3.13	AFM and Combined AFM-SECM Image on Fibroblasts . . .	86
3.14	Venturi Effect . . . . .	87
A.1	SEM Pictures of the Hole . . . . .	99
A.2	Pictures of the Fabricated Support . . . . .	99
A.3	Pictures of the Assembled Support . . . . .	100
B.1	SEM Pictures of the Fabricated Conductive Probe . . . . .	104
B.2	SEM Pictures of the Tip . . . . .	105

## **Part I**

# **Introduction**



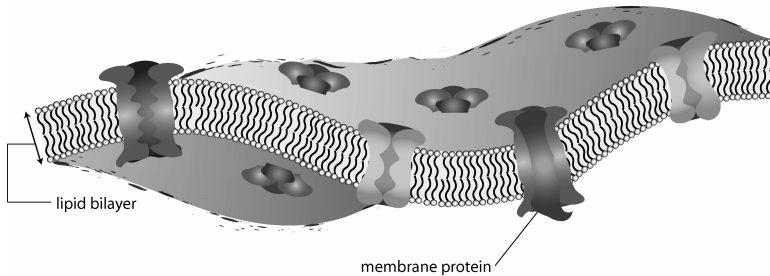
# Chapter 1

## Theory

This chapter will introduce the major principles and methods used for the presented work. Characterization of the microfabricated tools and experiments are presented in the core part which is based on publications in referred journals. The microfabrication of the different parts is then discussed in more detail in the appendix.

### 1.1 Cell Biology

All organisms consist of small cells, typically too small to be seen by naked eye, but big enough for an optical microscope . Each cell is a complex system consisting of many different building blocks enclosed in a membrane bag. There are unicellular (consisting only of one cell) and multicellular organisms. Bacteria and baker's yeast are examples of unicellular organisms able to survive and multiply independently in an appropriate environment. The human body contains about  $6 \times 10^{13}$  cells of about 320 different types. For instance there are several types of skin cells, muscle cells, brain cells (neurons), among many others. The cell size may vary depending on the cell type and circumstances. For instance, a human red blood cell is about 5 microns (0.005mm) in diameter, whereas neurons can be as long as 1m (from spinal cord to leg). Typically the diameter of an animal and plant cell is between 10 and 100 microns.



**Figure 1.1:** The fluid-mosaic model of the cell membrane.

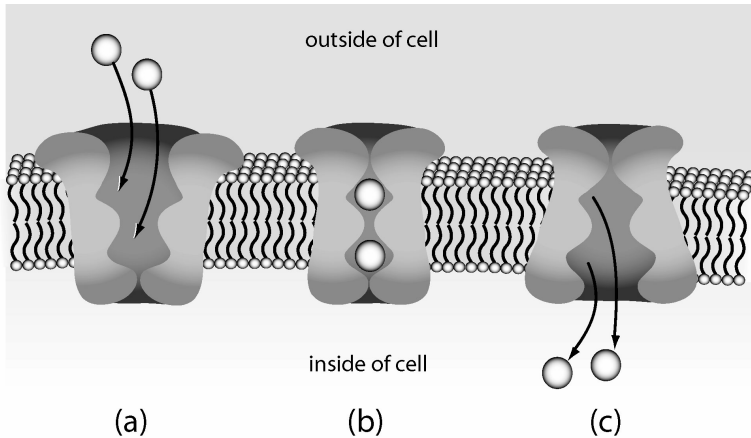
There are two types of organisms: eukaryotes and prokaryotes. Most organisms we see, such as trees, grass, flowers, weeds, worms, flies, mice, cats, dogs, humans are eukaryotes. Prokaryotes are single cellular organisms and are sometimes also known as microbes. Prokaryotic cells are smaller than eukaryotic cells (a typical size of a prokaryotic cell is about 1 micron in diameter) and have simpler structure. In both cases, a membrane separates the cell from the outside environment. As shown in figure 1.1 membranes are complex structures and an effective barrier to the environment. They regulate the flow of food, energy and information in and out of the cell. This will be detailed in the following section which is based on the textbook "Molecular Biology of the Cell".<sup>1</sup>

### 1.1.1 Cellular Transport

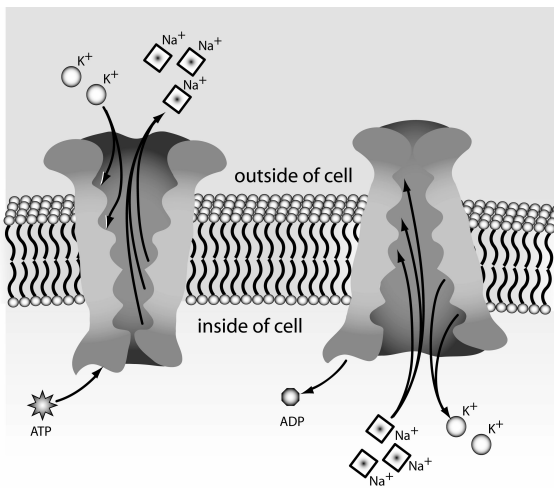
Cellular transport refers to the movement of compounds across the outer wall or membrane of the cell. This transport is critical in two respects. First, transport allows a cell to take in and release compounds in accordance with its biological function, i.e. uptake and release of oxygen by red blood cells. Second, it allows cells to regulate functions and activity, i.e. increased transport of glucose into muscle cells during activity. The cell membrane is primarily composed of a bilayer of various types of lipids and proteins. The two general characteristics of a molecule that will prevent it from passing through the membrane are size and polarity. Large molecules will not pass due to their size, and polar molecules will not pass both because of their



high affinity to the extra-cellular water molecules in which they are dissolved and because they cannot easily pass through the non polar membrane core. However, due to random vibrations occurring in the membrane, small polar molecules such as water can pass through. Triggered by diffusion, the net movement of molecules through the cell membrane occurs from regions of higher concentration to regions of lower concentration. For example, the flow or osmosis of water across a cell membrane will produce an equal concentration of solutes on both sides of the membrane. Therefore a cell will swell when placed in distilled water, and its membrane will eventually rupture. This would not be the case if the cell membrane would contain specific channel or transporter proteins which could equilibrate the solute concentration. These proteins facilitate the passage of a molecule across the membrane. In general, there are two types of transporters: Passive transporters, which do not need additional energy, and active transporters that generally employ energy in form of adenosine triphosphate (ATP) to drive the transport. Passive transporters, like glucose permease move molecules from higher concentration regions to lower concentration regions. The transport is believed to happen in three steps: binding, conformational change, release (figure 1.2). In the case of glucose permease the transport is reversible, thus it allows the passage of glucose molecules in both directions. An example of an active transporter that plays a very interesting physiological role is the sodium-potassium ATPase pump. In contrast to passive transporters, active transporters can move solute from areas of lower concentration to areas of higher concentration, hence against equilibrium. To achieve this, the transporter protein consume energy in form of ATP. The sodium-potassium ATPase pump transports more sodium ions out of the cell than potassium ions into the cell (figure 1.3). Therefore the exterior of the cell becomes positively charged relative to the interior of the cell. Thus the sodium-potassium ATPase pump maintains an ionic concentration difference, i.e. an electric potential, across the membrane. This so-called resting potential allows the propagation of electrical impulses along nerve cells and across synaptic clefts between nerve cells: An electrical signal causes voltage gated ion channels to open, enabling sodium and potassium ions to flow across the membrane. This results in a localized reversal of the electric potential to



**Figure 1.2:** The passive membrane transport is believed to happen in three steps: a) binding of the molecule, b) conformational change of the channel and c) release of the molecule.



**Figure 1.3:** Principle of the sodium-potassium ATPase pump, which uses the energy gained from the transformation of adenosine triphosphate (ATP) to adenosine diphosphate (ADP).

which neighboring ion channels respond and open, causing the electric potential to spread. As the sodium-potassium ATPase pump restores the resting potential after a short lag of time, the impulse travels towards the synapse like a wave. Once at the synapse the signal is transmitted via a neurotransmitter. Again the resting potential is restored by the sodium-potassium ATPase pump. When these pumps are not working properly, it takes a longer time to restore the resting potential, and an uncontrolled firing of additional nerve impulses occurs. This is the case for people diseased with myotonia, which is a so-called channelopathy. Diseases are only one of several motivations that drive scientists to investigate the function of channel proteins. The patch clamp technique is probably the most used procedure to gain insight in the behavior of membrane proteins. Atomic force microscopy (AFM) on the other hand, has been applied to measure the topography of membranes and to monitor topography changes.<sup>2</sup> These two techniques will be discussed in more depth in the following paragraphs.

## 1.2 Patch Clamp

In the previous section we saw one example of how the cell function can be linked to the electrical potential across its membrane. This potential, in turn, depends on the lipids and proteins of the membrane, such as ion channels and transporters. These kind of proteins are responsible for a variety of cell function. Consequently there is a great interest to understand how they work. The patch clamp technique is probably the most used method to study ion channels and transporter proteins. It basically consists of measuring the electric current through the mentioned proteins embedded in the cell membrane. This technique provides the means to study the state of the channels (open/close) in the time domain and to quantitatively determine the amount of ions transported across the membrane. This section introduces the basic concepts used in performing electrical experiments on cells and describes the tools used for making these measurements.

### 1.2.1 Electrical Potentials and Currents in Cells

The potential difference across a cell relates the potential of the cell's interior to that of the external solution, which, according to the commonly accepted convention, is zero.<sup>3</sup> This so-called resting potential is determined by the intracellular and extra cellular concentrations of ions to which the membrane is permeable in steady-state condition, i.e. with no net flow of electrical current across the membrane. The resting potential of most animal cells amounts to typically between 30 and 90mV, and reaches between 150 and 200mV in plant cells.<sup>3</sup> These potential differences and the resulting electrical currents are measured in electrophysiological experiments in biological systems. Usually, the measured currents range from picoamperes to microamperes. For instance if, typically,  $10^4 Na^+$  ions cross the membrane per open  $Na^+$  channel and millisecond, this current amounts to 1.6pA ( $1.6 \cdot 10^{-19} C/ion \cdot 10^4 ions/ms \cdot 10^3 ms/s$ ). Generally, electric currents flow through resistors or conductors. The two terms are complementary: the former emphasizes the barriers to current flow, while the latter emphasizes the pathways of current flow. In electrophysiology, a closed ion channel can be approximated by a resistor and an open channel by a conductor.<sup>3,4</sup> However, ion channels are non ohmic and show a nonlinear relation between current and voltage, when opened.<sup>4</sup>

For measuring electrical currents in electrophysiology the sensing interface of the measuring instrument to the liquid environment of the biological cells is a metallic electrode. At the electrode, the electrochemical current is transformed from a flow of electrons in the wire to a flow of ions in solution or vice versa. The choice of the electrode thus plays an important role in electrophysiological measurements.

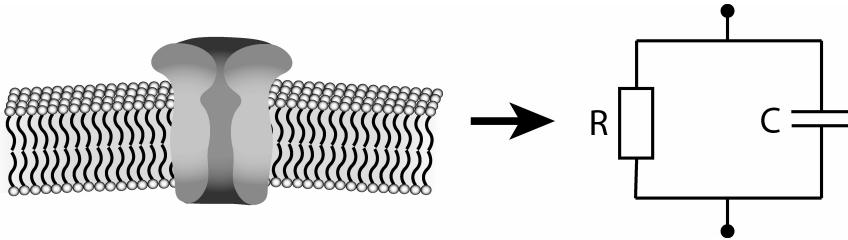
### 1.2.2 Electrodes

Several types of electrodes are used in electrophysiological measurements. The most common one is a silver/silver chloride electrode (Ag/AgCl), which is a silver wire coated with silver chloride. The Ag/AgCl electrode performs well only in solutions containing chloride ions. If electrons flow from the copper wire through the silver wire to the electrode AgCl pellet, they convert

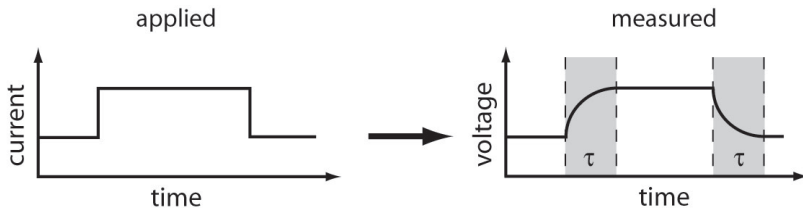
the AgCl to Ag atoms and the  $\text{Cl}^-$  ions become hydrated and enter the solution. If electrons flow in the reverse direction, Ag atoms in the silver wire that is coated with AgCl oxidize (one electron per atom) and combine with  $\text{Cl}^-$  ions that are in the solution to make insoluble AgCl.<sup>5,6</sup> Therefore, this is a reversible electrode, i.e., current can flow in both directions. The major drawback of Ag/AgCl electrodes is that the AgCl can be completely consumed by the current flow. In this case bare silver could come in contact with the solution and silver ions leaking from the wire could poison many proteins.<sup>6</sup> Also, the measurement becomes dominated by unpredictable, poorly reversible surface reactions due to other ions in the solution and trace impurities in the silver.<sup>5</sup> Other frequently used types of electrodes are made of platinum (Pt). Compared to the Ag/AgCl, Pt electrodes aren't exhaustible, however, their reaction is not reversible.<sup>6</sup>

### 1.2.3 Capacitors in Cells

Biological membranes are typically less than 10nm thick. Consequently, a transmembrane resting potential of about 100mV produces a very sizable electrical field of about  $10^5\text{V/cm}$  across the membrane. This is close to the value at which most insulators irreversibly break down because their atoms become ionized. Changes in these transmembrane fields are presumably sensed by the gating domains of voltage-sensitive ion channels and determine their opening and closing.<sup>3,4</sup> Therefore, the ion channels limit the electric field across the cell membrane. Another consequence of the membrane's thickness is that it makes an excellent capacitor. As the capacitance is proportional to the area, the membrane capacitance increases with cell size. Most lipid bilayer membranes of cells have a capacitance of  $1\mu\text{F/cm}^2$  ( $0.01\text{pF}/\mu\text{m}^2$ ).<sup>3,7</sup> As long as the voltage across a membrane remains constant, one can ignore the effect of the membrane capacitance on the currents flowing across the membrane through ion channels. However, when the voltage changes, there are transient capacitive currents in addition to the steady-state currents through the conductive channels. These capacitive currents have a major influence on the time-dependent electrical properties of cells. It is important to keep in mind that the stored charge

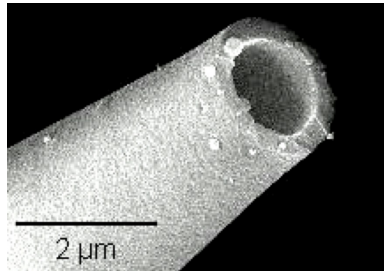


**Figure 1.4:** The electrical behavior of an ion channel in a cell membrane can be represented by a resistance in parallel with a capacitor.



**Figure 1.5:** Changes in voltage across the membrane are dominated by the high capacitance of the lipid bilayer membrane. Thus a voltage pulse is delayed by the time constant defined by the equivalent RC circuit.

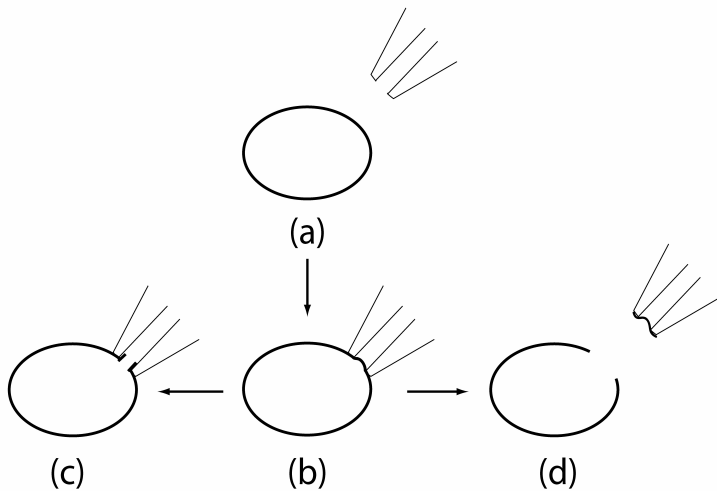
on the membrane capacitance accompanies the resting potential and any change in the voltage across the membrane is accompanied by a change in this stored charge. Indeed, if a current is applied to the membrane, either by channels elsewhere in the cell or by current from the electrode, this current first satisfies the requirement for charging the membrane capacitance, then it changes the membrane voltage. Formally, this can be shown by representing the membrane as a resistor of value  $R$  in parallel with capacitance  $C$  (figure 1.4). Thus like in a RC circuit, changes in the membrane voltage are not reached immediately. Instead, they are approached with the time constant  $\tau$ , given by  $\tau = RC$  (figure 1.5). Therefore when the duration impulse is less than  $\tau$  the specific activation threshold voltage might not be reached.



**Figure 1.6:** SEM micrograph of a patch clamp micro pipette. The inner diameter is  $1\mu m$

#### 1.2.4 Current Clamp and Voltage Clamp

In a current-clamp experiment, one applies a known constant or time-varying current and measures the change in membrane potential caused by the applied current. This type of experiments are often used to mimic the current produced by a synaptic input.<sup>5</sup> In a voltage clamp experiment one controls the membrane voltage and measures the trans-membrane current required to maintain that voltage.<sup>5</sup> The patch clamp technique is a special voltage clamp that aims to resolve currents flowing through single ion channels. Compared to the voltage clamp, the currents recorded during the patch clamp experiences are of the order of picoamperes in single-channel recording and usually up to several nanoamperes in whole-cell recording. The patch clamp technique is applied in different configurations. It consists of carefully placing a pulled glass micro pipette (figure 1.6) on the membrane of a living cell (figure 1.7a). The part of the cell membrane within the inner diameter of the micro pipette extremity is called patch. By applying a gentle suction to the pipette, the membrane patch forms a tight seal with the glass pipette. The electrical characteristics can now be investigated with the help of an electrode inserted in the solution filled glass micro pipette and a second electrode in the bath. This is the so-called cell-attached configuration (figure 1.7b), where the cell remains intact. When a higher suction is applied to the pipette, the patch can be broken. This is the so-called whole-cell configuration, which enables to characterize the



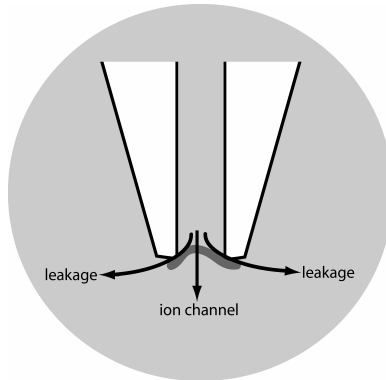
**Figure 1.7:** Three different patch clamp configurations: a) the pipette approaches the biological cell; b) cell-attached configuration; c) whole-cell configuration; d) inside-out configuration.

whole cell membrane (figure 1.7c). If after reaching the cell-attached configuration, the patch wasn't broken, but the pipette is taken off gently from the cell, the part of the membrane present under the pipette extremity is separated from the cell and remains on the pipette. The formerly internal side of the cell membrane is now pointing outwards into the solution, while the formerly outside of the membranes now inside the pipette. This is the so-called inside-out configuration (figure 1.7d).

### 1.2.5 Glass Microelectrodes and Tight Seals

Successful electrophysiological measurements strongly depend on the fabrication and quality of the glass micro pipettes. Successful patch recording requires a tight seal between the pipette and the membrane.<sup>7,8</sup> Although there is not yet a satisfactory molecular description of this seal, we can describe its electrical characteristics: The quality of the measurement depends on minimizing perturbations of the cells. For the case of patch re-





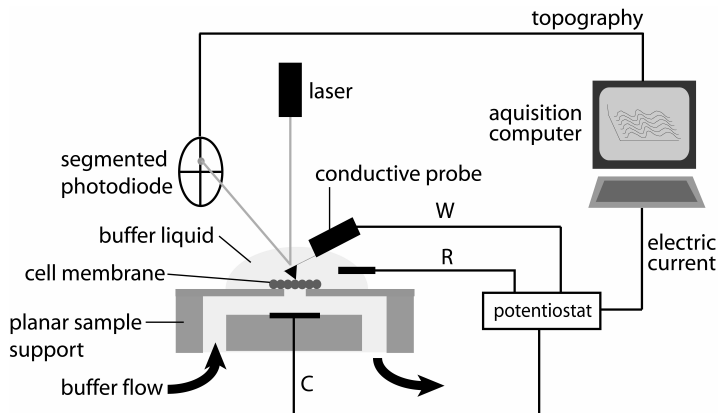
**Figure 1.8:** Leakage current for a badly sealed cell membrane patch induces additional noise in the measurement.

ording, currents through the seal do not distort the measured voltage or current, but they do add noise to the current (figure 1.8). If a current of  $N$  ions/ms passes through an open channel, then the current will fluctuate with a standard deviation of  $\sqrt{N}$ . These fluctuations produce noise on the single-channel recorded traces. If a leakage current is flowing in parallel through the seal it causes an increase in the standard deviations. For instance, if the current through the seal is ten-fold larger than through the channel, then the statistical fluctuations in current flow produced by the seal are  $\sqrt{10}$  (316%) larger than they would be for a "perfect" seal.

### 1.3 Combining AFM and Patch Clamp

In the beginning, atomic force microscopy<sup>9</sup> (AFM) was mostly applied to hard materials to analyze the topographical, electrical, magnetic, thermal and elastic properties. Soon after, the AFM started also to be used for the characterization of the surface of living cells and biomembranes.<sup>2,10-12</sup> Today AFM is commonly used to study the elastic and plastic properties of cultured cells,<sup>13-16</sup> to directly image neurons and glia<sup>17</sup> and even to study the binding forces between individual molecules and their subunits respec-

tively.<sup>18</sup> AFM has also directly been combined with the patch clamp technique.<sup>19–23</sup> Using an AFM probe with a tip diameter of only few nanometers it was possible to displace individual stereocilia of cochlear hair cells resulting in opening of single transduction channels.<sup>24</sup> However, AFM experiments on the tip apex of a patch clamp micropipette are quite demanding in matters of complexity and stability of the setup.<sup>23</sup> Therefore the aim of this work is to fabricate dedicated tools to facilitate the combination of AFM and patch clamp techniques in a conventional AFM setup. Figure 1.9 shows the schematic representation of the proposed setup. To fit the requirements of AFM, the conventional patch clamp pipette was replaced by a planar sample support featuring a sub micrometer scaled patch site (aperture) and an integrated electrode. The sensing electrode is integrated at the tip of a special conductive AFM probe. In combination with a reference electrode the electric currents are measured by a potentiostat and the topography is acquired by a conventional laser feedback system. This setup should thus be capable of simultaneously acquire the topography and map the electrical properties of cell membranes. Indeed, the setup needs to fulfill special requirements: The materials used to fabricate the planar sample support need to be biocompatible or at least not toxic. To ensure a good seal between membrane and support and to achieve high resolution images of the membrane patches, the upper surface of the support should be smoother than the observed biological sample, i.e. posses a mean roughness below 1nm. A small patch site ( $< 1\mu m$ ) further improves the sealing and makes imaging on suspended membranes less critical. In addition, the total capacity of the sample support should preferably be smaller than the capacity of the investigated cell, in order to not further increase the RC time constant of the system (figure 1.5). As cell membranes are soft and fragile the force applied by the conductive AFM probe needs to be as small as possible, i.e. the probes need to have spring constants below 0.1N/m. In order to keep cells alive, they need to be held in physiological buffer, therefore all measurements must to be performed in liquid. To obtain local electric information in liquid, the exposed portion of the metal electrode of the used probes need to be as small as possible. Also here, all materials used for microfabrication need to be non toxic. This is especially the case for the metal electrode as it

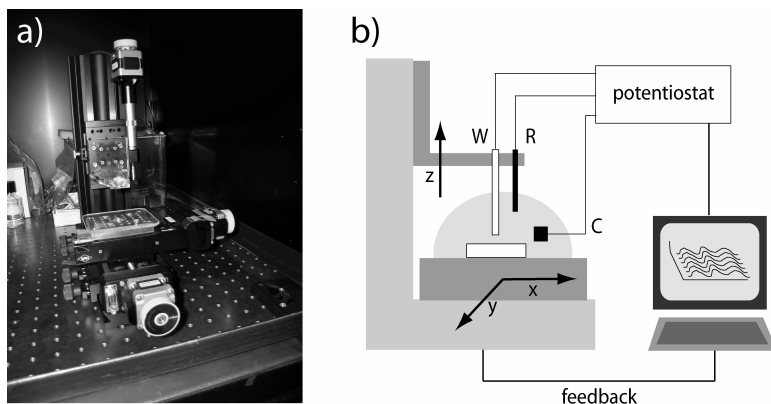


**Figure 1.9:** Schematic representation of the combined AFM- patch clamp setup. The AFM probe simultaneously acquires topography and electrical characteristics of the observed sample. The electric currents are measured by a three electrode system, i.e. W = working, C = counter and R= reference electrode.

will be in contact with biological materials. In addition the electrodes need to be electrochemically characterized. During the electrochemical characterization I realized the geometrical similarity of the conductive AFM probe to the probes used in scanning electrochemical microscopy (SECM). The following paragraph will introduce SECM and elucidate the advantage of combining it with AFM.

## 1.4 Scanning Electrochemical Microscopy

SECM is a scanning probe microscope (SPM) like atomic force microscopes (AFM),<sup>9</sup> but more related to the familiar scanning tunneling microscopes (STM). SECM allows to map in-situ the topography of surfaces that are immersed into liquids as well as a visualization of spatially-confined variations in the chemical reactivity.<sup>25,26</sup> Typically imaging occurs in an electrolyte solution with an electrochemically active mediator, e.g. redox agent. In most cases, the SECM sensor is an ultra micro electrode (UME)<sup>25</sup> and the signal is a faradaic current. The chemical sensitivity of the UME and the use of



**Figure 1.10:** a) Homemade SECM realized by V. Auger and M. Koudelka-Hep; b) Schematic representation of the SECM: Working (W), Reference (R) and Counter (C) electrodes are connected to the potentiostat. The PC reads out the values measured by the potentiostat and controls the UME sample distance by a feedback system. The stepper motors for the x, y and z displacement are also PC controlled.

solution phase ions or molecules as the imaging signal, distinguishes SECM from related methods such as electrochemical STM or AFM.

### 1.4.1 Instrumentation

The SECM (figure 1.10) uses stepper motors to position the UME in any-one of its 3 orthogonal axes. In addition the positioners allow movements between 0.1 and 300  $\mu\text{m}$  during SECM imaging. Often the UME and substrate potential must be simultaneously controlled while the faradaic current flow is monitored during imaging. This is enabled by means of a bi-potentiostat.

### 1.4.2 Electrodes

Undoubtedly, the most crucial component of the SECM is the UME. Since the achievable spatial resolution of SECM imaging strongly depends on the shape and size of the electrochemically active UME.<sup>25,27–29</sup> Its basic implementation is a metal disc, having one side exposed to the electrolyte and

the rest being embedded in an insulator (figure 1.11). Such UMEs have been widely used in electroanalytical chemistry and SPM techniques. The quality of the insulation is essential for producing a good probe.<sup>30</sup> UMEs are commonly made by heat sealing microscopic wires (gold, platinum, and carbon) into glass tubes. The end is then polished to expose the embedded end of the wire. In addition different coating materials have been used: electropolymerisation,<sup>31,32</sup> electrophoretic deposition,<sup>33–36</sup> RF sputtering,<sup>37</sup> dip-coating in varnish<sup>38,39</sup> or paraffin,<sup>40</sup> translation through a bead of molten glass,<sup>41</sup> poly(alpha-methylstyrene),<sup>42</sup> apiezon wax<sup>43,44</sup> and perfluoropolyether.<sup>45</sup> Typically the metal disc of a UME has a radius of 5 to 25  $\mu\text{m}$ . An insulator radius of 3 to 10 times the electrode radius is desirable.<sup>46</sup>

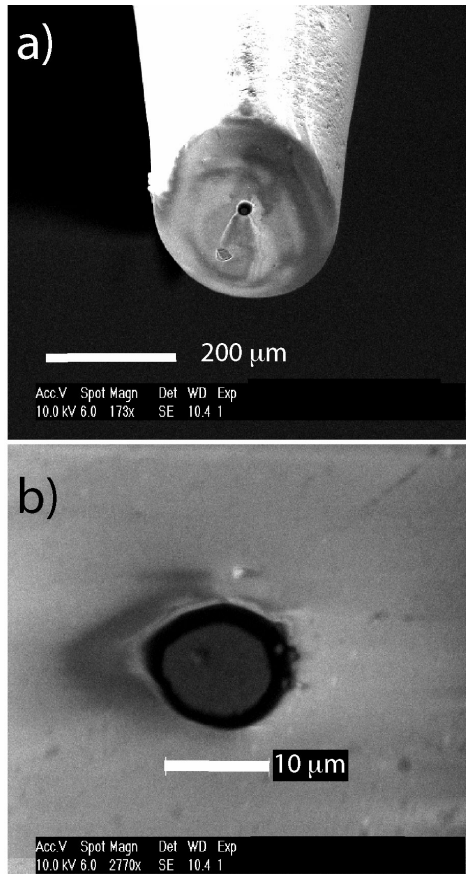
### 1.4.3 SECM Imaging

A requirement of all SPM techniques is that the signal probed by the tip must be influenced in a reproducible way by the presence of the surface of the sample under investigation. In addition this interaction should strongly depend on the probe sample distance. This will allow to take constant interaction contour plots by means of a feedback mechanism which stabilizes the interaction. In SECM the two major imaging methods are the "feedback" and "generation/collection" (G/C) methods.

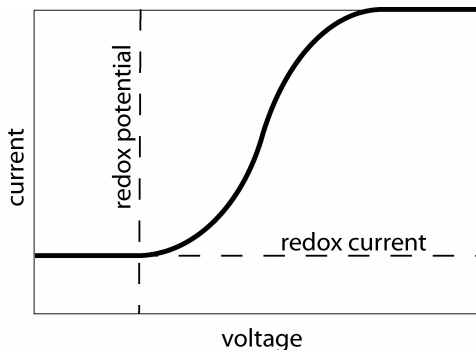
#### Feedback Imaging

The unique voltammetric response of ultra micro electrodes, or UMEs, are an essential part of the SECM feedback or G/C methods.<sup>25,26</sup> Shown in figure 1.12 is a idealized cyclic voltammogram (CV) when the UME is at a large distance from the substrate (i.e. several UME diameters away). The curve shows that the current reaches a plateau from a certain voltage on. Between this voltage and the point of hydrolysis the faraday current ( $I_{T,\infty}$ ) caused by the electrochemical conversion of the redox active species, is independent of voltage and time.<sup>25</sup>

This faraday current provides the signal, which is exploited in the feedback mode of SECM imaging. When the UME is brought very close to a surface,



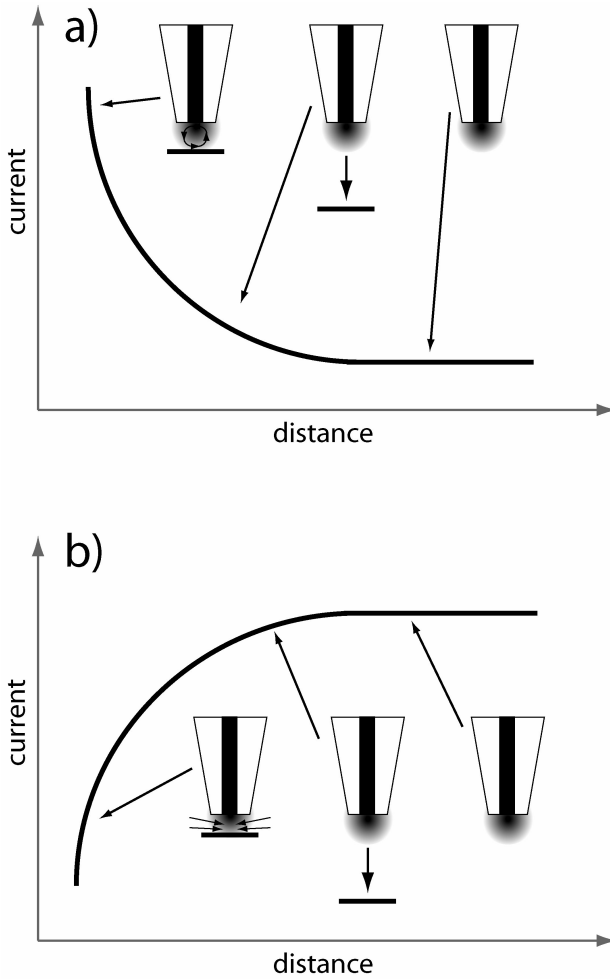
**Figure 1.11:** a) SEM micrograph of a  $5\mu\text{m}$  disc ultra micro electrode; b) Zoom onto the metal disc.



**Figure 1.12:** Schematic cyclic voltammogram.

this electrochemical signal is perturbed in a characteristic way for electrochemically active or passive surface, respectively. Negative Feedback (figure 1.13b) occurs through physically blocking the diffusion of mediator molecules to the UME by an electrochemically passive surface. This results in a current drop, when reducing the the distance to the sample. In contrast, the positive feedback (figure 1.13a) process occurs when the redox active mediator is restored to its original oxidation state at the substrate by an electrochemical, chemical, or enzymatic reaction. As the distance to the electrochemically active surface decreases, the local concentration of converted mediator at the UME increases. Thus, the regeneration of the mediator between UME and substrate becomes more efficient and the current  $I_T$  increases. Positive and negative feedback modes are extreme situations which define the contrast of the electrochemical feedback image and are highly distance-dependent. Approach curves (figure 1.13) can be used to position the UME at an appropriate working distances inside the regime of the electrochemical "near field".

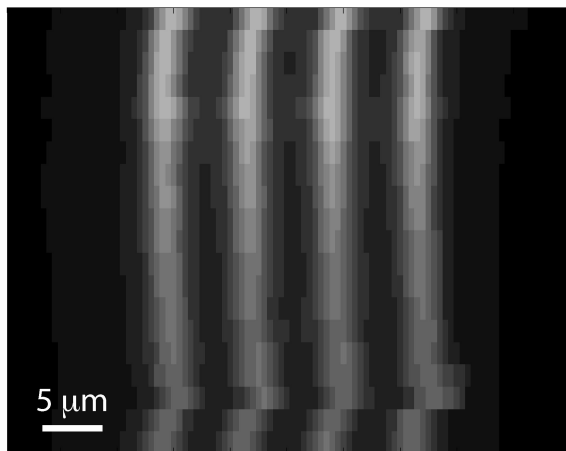
A three-dimensional SECM image (figure 1.14) is obtained by scanning the UME in the x-y plane at a user-defined fixed height above the sample and monitoring the UME current,  $I_T$ , as a function of the UME location. A particular advantage of SECM in imaging applications, compared to other types of scanning probe microscopy, is that the observed response can be in-



**Figure 1.13:** Schematic SECM approach curves: a) Positive feedback; b) Negative feedback.



terpreted based on fairly rigorous theory,<sup>25,27–29</sup> and hence the measured current can be employed to estimate the UME-substrate distance. A further advantage of the SECM is the ability to design experiments in which the chosen mediator can be used to provide chemical and electrochemical activity maps with micrometer resolution. However, constant-height SECM imaging has limits on heterogeneous surfaces with variations in both, conductivity and topography since current changes associated to distance variations cannot simply be distinguished from those due to alterations in conductivity. Furthermore, the UME's are easily crashed into the sample without a distance control on tilted or rough surfaces. This is especially the case when decreasing the size of the UME for imaging at higher resolution. A solution to these limitations can be achieved by combining SECM with other



**Figure 1.14:** Real SECM micrograph on  $5\mu\text{m}$  wide and  $5\mu\text{m}$  spaced gold lines deposited on silicon dioxide and connected as counter electrode. There is a clear difference between the positive feedback on the gold lines and the negative feedback on the silicon dioxide. The measurement was made with the SECM shown in figure 1.10 and with the UME shown in figure 1.11.

SPM techniques, i.e. AFM.<sup>47</sup>

### Generation/Collection Imaging

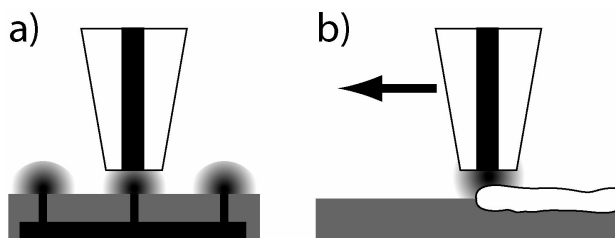
In the generation/collection (GC) mode (figure 1.15a), the signal arises from a species generated at the surface of the imaged material. Ideally, the UME acts only as a passive sensor with the ability to produce concentration maps of a particular chemical species near the substrate surface. In amperometric GC, the electro active species emitted, "generated", by the substrate are detected, "collected", at an UME.

#### 1.4.4 Surface Modification by SECM

In addition to imaging, the UME can be a microscopic source or sink of electrons and chemical reagents. With the UME positioned close to surface, these chemical reagents react at the surface on a microscopic scale (figure 1.15b), turning the SECM into a versatile microfabrication device.

#### 1.4.5 SECM Applications

This section will give an overview on several application of SECM in its different operation modes.



**Figure 1.15:** a) Generation Collection Mode: the UME is sensing the mediator diffusing through pores; b) Surface Modification by SECM: local electrochemical oxidation.

### **Characterization of Thin Films and Membranes**

SECM is a useful technique for studying thin films on interfaces. For example, polyelectrolytes, electronically conductive polymers, passivation films on metals and dissolution processes have been extensively investigated by SECM.<sup>48-74</sup> Another interesting applications of SECM is the study of charge transport at the interface between two immiscible electrolyte solution.<sup>75-82</sup> Unlike conventional techniques, SECM allows for studying both ion and electron transfer at the interface.

### **Generation Collection Mode in Medicine and Biology**

Generation Collection Mode SECM has been used to spatially resolved quantitative measurement of ion flux through porous material such as mouse skin or dental material. In particular SECM has been actively employed to probe artificially or naturally patterned biological systems.<sup>83-93</sup> In addition, SECM also showed the ability to image an enzymatic reaction over a localized surface region.<sup>94</sup>

### **Electrochemical Patterning**

Electrolytic generation of an oxidizing agent at the UME can precisely etch metal and semiconductor surfaces. Local pH changes caused by an electrochemical reaction at the UME have been used to deposit metal oxides and polymers. Deposition of metal and polyaniline lines as thin as 0.3  $\mu\text{m}$  has been reported.<sup>95</sup>

---

## Bibliography

1. Alberts, B.; Johnson, A.; Lewis, J.; Raff, M.; Roberts, K.; Walter, P. *Molecular Biology of the Cell*; Garland Science Taylor and Francis Group: New York, NY, 2002.
2. Engel, A.; Mueller, D. ; Observing single biomolecules at work with the atomic force microscope, *Nat. Struct. Biol.* **2000**, *7*, 715-718.
3. Hille, B.; Aldrich, R. ; Ionic Channels in Excitable Membranes, *Science* **1985**, *228*, 867-868.
4. Miller, C. *Ion Channel Reconstitution*; Plenum Press: New York, NY, 1986.
5. Smith, T. G.; Lecar, H.; Redman, S. J.; Gage, P. W. *Voltage and Patch Clamping with Microelectrodes*; American Physiological Society: Bethesda, MD, 1985.
6. Standen, N. B.; Gray, P. T. A.; Whitaker, M. J. *Microelectrode Techniques: The Plymouth Workshop Handbook*; The Company of Biologists Limited: Cambridge, England, 1987.
7. Ypey, D. L.; DeFelice, L. J. *The Patch-Clamp Technique*; Vanderbilt University Medical Center Press: Vanderbilt, 1999.
8. Brown, K. T.; Flaming, D. G. *Advanced Micropipette Techniques for Cell Physiology*; John Wiley and Sons: New York, NY, 1986.
9. Binnig, G.; Quate, C. F.; Gerber, C. ; Atomic Force Microscope, *Phys. Rev. Letts.* **1986**, *56*, 930-933.
10. Hörber, J. K. H.; Häberle, W.; Ohnesorge, F.; Binnig, G.; Liebich, H. G.; Czerny, C.; Mahnel, H.; Mayr, A. ; Investigation of Living Cells in the Nanometer Regime with the Scanning Force Microscope, *Scanning Microsc.* **1992**, *6*, 919-930.

11. Haydon, P. G.; Lartius, R.; Parpura, V.; MarcheseRagona, S. P. ; Membrane deformation of living glial cells using atomic force microscopy, *J. Microsc.-Oxf.* **1996**, *182*, 114-120.
12. Mueller, D. J.; Fotiadis, D.; Scheuring, S.; Mueller, S. A.; Engel, A. ; Electrostatically balanced subnanometer imaging of biological specimens by atomic force microscope, *Biophys. J.* **1999**, *76*, 1101-1111.
13. Radmacher, M.; Fritz, M.; Cleveland, J. P.; Walters, D. A.; Hansma, P. K. ; Imaging Adhesion Forces and Elasticity of Lysozyme Adsorbed on MICA with the Atomic-Force Microscope, *Langmuir* **1994**, *10*, 3809-3814.
14. Schönenberger, C. A.; Hoh, J. H. ; Slow Cellular-Dynamics in MDCK and R5 Cells Monitored by Time-Lapse Atomic-Force Microscopy, *Biophys. J.* **1994**, *67*, 929-936.
15. Shroff, S. G.; Saner, D. R.; Lal, R. ; Dynamic Micromechanical Properties of Cultured Rat Atrial Myocytes Measured by Atomic-Force Microscopy, *Am. J. Physiol.-Cell Physiol.* **1995**, *38*, C286-C292.
16. Alonso, J. L.; Goldmann, W. H. ; Feeling the forces: atomic force microscopy in cell biology, *Life Sciences* **2003**, *72*, 2553-2560.
17. Parpura, V.; Haydon, P. G.; Henderson, E. ; 3-Dimensional Imaging of Living Neurons and Glia with the Atomic Force Microscope, *J. Cell Sci.* **1993**, *104*, 427-432.
18. Florin, M.; Rief, M.; Lehmann, H.; Ludwig, M.; Dornmair, C.; Moy, V. T.; Gaub, H. E. ; Sensing Specific Molecular-Interactions with the Atomic-Force Microscope, *Biosens. Bioelectron.* **1995**, *10*, 895-901.
19. Besch, S.; Snyder, K. V.; Zhang, R. C.; Sachs, F. ; Adapting the Quesant (c) Nomad (TM) atomic force microscope for biology and patch-clamp atomic force microscopy, *Cell Biochem. and Biophys.* **2003**, *39*, 195-210.

20. Kiss, L.; Bennett, P. B.; Uebele, V. N.; Koblan, K. S.; Kane, S. A.; Neagle, B.; Schroeder, K. ; High throughput ion-channel pharmacology: Planar-array-based voltage clamp, *Assay Drug Dev. Technol.* **2003**, *1*, 127-135.
21. Roland, G.; Kepplinger, K. J. F.; Zhu, R.; Maulet, Y.; Groschner, K.; Soldatov, N. M.; Hinterdorfer, P.; Romanin, C. ; A combined approach of patch clamp and AFM for studying Ca<sup>2+</sup>-dependent inactivation of class C-type Ca<sup>2+</sup> channels, *Biophys. J.* **2002**, *82*, 105A-106A.
22. Danker, T.; Mazzanti, M.; Tonini, R.; Rakowska, A.; Oberleithner, H. ; Using atomic force microscopy to investigate patch-clamped nuclear membrane, *Cell Biol. Int.* **1997**, *21*, 747-757.
23. Mosbacher, J.; Haeberle, W.; Hoerber, J. ; Studying membranes with scanning force microscopy and patch-clamp technique, *J. Vac. Sci. Technol. B* **1996**, *14*, 1449-1452.
24. Langer, M. G.; Koitschev, A.; Fink, S. ; Combined AFM and patch clamp: A tool for investigation of single mechanosensitive ion channels in the inner ear, *Biophys. J.* **2005**, *88*, 154A-154A.
25. Bard, A. J.; Mirkin, M. V. *Scanning Electrochemical Microscopy*; Marcel Dekker: New York, NY, 2001.
26. Bard, A. J.; Faulkner, L. R. *Electrochemical Methods, Fundamentals and Applications*; Wiley and Sons: New York, NY, 2001.
27. Bard, A. J.; Fan, F. R. F.; Kwak, J.; Lev, O. ; Scanning Electrochemical Microscopy. Introduction and Principles., *Anal. Chem.* **1989**, *61*, 132-138.
28. Zoski, C. G. ; Ultramicroelectrodes: Design, fabrication, and characterization, *Electroanalysis* **2002**, *14*, 1041-1051.
29. Zoski, C. G.; Liu, B.; Bard, A. J. ; Scanning electrochemical microscopy: Theory and characterization of electrodes of finite conical geometry, *Anal. Chem.* **2004**, *76*, 3646-3654.

30. Zoski, C. G.; Mirkin, M. V.; Steady-state limiting currents at finite conical microelectrodes, *Anal. Chem.* **2002**, *74*, 1986-1992.
31. Strein, T. G.; Ewing, A. G.; Characterization of Submicron-Sized Carbon Electrodes Insulated with a Phenol Allylphenol Copolymer, *Anal. Chem.* **1992**, *64*, 1368-1373.
32. Potje-Kamloth, K.; Janata, J.; Josowicz, M.; Electrochemically prepared insulation for carbon fiber microelectrodes, *Ber. Bunsenges. Phys. Chem.* **1989**, *93*, 1480-1491.
33. Bach, C. E.; Nichols, R. J.; Beckmann, W.; Meyer, H.; Schulte, A.; Besenhard, J. O.; Jannakoudakis, P. D.; Effective Insulation of Scanning-Tunneling-Microscopy Tips for Electrochemical Studies Using an Electropainting Method, *J. Electrochem. Soc.* **1993**, *140*, 1281-1284.
34. Schulte, A.; Chow, R. H.; Cylindrically etched carbon-fiber microelectrodes for low-noise amperometric recording of cellular secretion, *Anal. Chem.* **1998**, *70*, 985-990.
35. Slevin, C. J.; Gray, N. J.; Macpherson, J. V.; Webb, M. A.; Unwin, P. R.; Fabrication and characterisation of nanometre-sized platinum electrodes for voltammetric analysis and imaging, *Electrochem. Commun.* **1999**, *1*, 282-288.
36. Conyers, J. L.; White, H. S.; Electrochemical characterization of electrodes with submicrometer dimensions, *Anal. Chem.* **2000**, *72*, 4441-4446.
37. Abe, T.; Itaya, K.; Uchida, I.; An Electrochemical Fabrication Method for Gold and Carbon Ultramicroelectrode, *Chem. Lett.* **1988**, 399-402.
38. Gewirth, A. A.; Craston, D. H.; Bard, A. J.; Fabrication and Characterization of Microtips for Insitu Scanning Tunneling Microscopy, *J. Electroanal. Chem.* **1989**, *261*, 477-482.

39. Vitus, C. M.; Chang, S. C.; Schardt, B. C.; Weaver, M. J. ; Insitu Scanning Tunneling Microscopy as a Probe of Adsorbate-induced Reconstruction at Ordered Monocrystalline Electrodes - Co on Pt (100), *J. Phys. Chem.* **1991**, *95*, 7559-7563.
40. Zhang, B. L.; Wang, E. K. ; Fabrication of STM Tips with Controlled Geometry by Electrochemical Etching and ECSTM Tips Coated with Paraffin, *Electrochim. Acta* **1994**, *39*, 103-106.
41. Penner, R. M.; Heben, M. J.; Longin, T. L.; Lewis, N. S. ; Fabrication and use of Nanometer-Sized Electrodes in Electrochemistry, *Science* **1990**, *250*, 1118-1121.
42. Penner, R. M.; Heben, M. J.; Lewis, N. S. ; Preparation and Electrochemical Characterization of Conical and Hemispherical Ultramicroelectrodes, *Anal. Chem.* **1989**, *61*, 1630-1636.
43. Nagahara, L. A.; Thundat, T.; Lindsay, S. M. ; Preparation and Characterization of STM Tips for Electrochemical Studies, *Rev. Sci. Instrum.* **1989**, *60*, 3128-3130.
44. Mirkin, M. V.; Fan, F. R. F.; Bard, A. J. ; Scanning Electrochemical Microscopy. 13. Evaluation of the Tip Shape of Nanometer Size Microelectrodes, *J. Electroanal. Chem.* **1992**, *328*, 47-62.
45. Liu, B.; Rolland, J. P.; DeSimone, J. M.; Bard, A. J. ; Fabrication of ultramicroelectrodes using a "Teflon-like" coating material, *Anal. Chem.* **2005**, *77*, 3013-3017.
46. Ciani, I.; Daniele, S. ; Voltammetric Determination of the Geometrical Parameters of Inlaid Microdisks with Shields of Thickness Comparable to the Electrode Radius, *Anal. Chem.* **2004**, *76*, 6575-6581.
47. Gullo, M. R.; Frederix, P. L. T. M.; Akiyama, T.; Engel, A.; de Rooij, N. F.; Stauer, U. ; Characterization of Batch Fabricated Probes for Combined Atomic Force and High Resolution Scanning Electrochemical Microscopy, *Anal. Chem.* **2006**, *78*, 5436-5442.



48. Lee, C.; Bard, A. J. ; Scanning Electrochemical Microscopy - Application to Polymer and Thin Metal-Oxide Films, *Anal. Chem.* **1990**, *62*, 1906-1913.
49. Lee, C.; Kwak, J. Y.; Anson, F. C. ; Application of Scanning Electrochemical Microscopy to Generation/Collection Experiments with High Collection Efficiency, *Anal. Chem.* **1991**, *63*, 1501-1504.
50. Kwak, J. Y.; Lee, C.; Bard, A. J. ; Scanning Electrochemical Microscopy. 5. A Study of the Conductivity of Polypyrrole Film, *J. Electrochem. Soc.* **1990**, *137*, 1481-1484.
51. Lee, C.; Anson, F. C. ; Use of Electrochemical Microscopy to Examine Counterion Ejection from Nafion Coatings on Electrodes, *Anal. Chem.* **1992**, *64*, 528-533.
52. Jeon, I. C.; Anson, F. C. ; Application of Scanning Electrochemical Microscopy to Studies of Charge Propagation within Polyelectrolyte Coatings on Electrodes, *Anal. Chem.* **1992**, *64*, 2021-2028.
53. Mirkin, M. V.; Fan, F. R. F.; Bard, A. J. ; Direct Electrochemical Measurements Inside a 2000-Angstrom Thick Polymer Film by Scanning Electrochemical Microscopy, *Science* **1992**, *257*, 364-366.
54. Arca, M.; Mirkin, M. V.; Bard, A. J. ; Polymer-Films on Electrodes. 26. Study of Ion-Transport and Electron-Transfer at Polypyrrole Films by Scanning Electrochemical Microscopy, *J. Phys. Chem.* **1995**, *99*, 5040-5050.
55. Pyo, M.; Bard, A. J. ; Scanning electrochemical microscopy .35. Determination of diffusion coefficients and concentrations of Ru(NH<sub>3</sub>)<sub>6</sub>(3+) and methylene blue in polyacrylamide films by chronoamperometry at ultramicrodisk electrodes, *Electrochim. Acta* **1997**, *42*, 3077-3083.
56. Scott, E. R.; Laplaza, A. I.; White, H. S.; Phipps, J. B. ; Transport of Ionic Species in Skin: Contribution of Pores to the Overall Skin Conductance, *Pharm. Res.* **1993**, *10*, 1699-1709.

- 
57. Snyder, S. R.; White, H. S. ; The Role of Redox Chemistry in Scanning-Tunneling-Microscopy Imaging of Electroactive Films, *J. Electroanal. Chem.* **1995**, *394*, 177-185.
  58. Basame, S. B.; White, H. S. ; Scanning Electrochemical Microscopy of Native Titanium-Oxide Films - Mapping the Potential Dependence of Spatially-Localized Electrochemical Reactions, *J. Phys. Chem.* **1995**, *99*, 16430-16435.
  59. Casillas, N.; Charlebois, S.; Smyrl, W. H.; White, H. S. ; Pitting Corrosion of Titanium, *J. Electrochem. Soc.* **1994**, *141*, 636-642.
  60. Wipf, D. O. ; Initialization and Study of Localized Corrosion by Scanning Electrochemical Microscopy, *Colloid Surf. A-Physicochem. Eng. Asp.* **1994**, *93*, 251-261.
  61. Scott, E. R.; White, H. S.; Phipps, J. B. ; Direct Imaging of Ionic Pathways in Stratum-Corneum Using Scanning Electrochemical Microscopy, *Solid State Ion.* **1992**, *53-6*, 176-183.
  62. Nugues, S.; Denuault, G. ; Scanning electrochemical microscopy: Amperometric probing of diffusional ion fluxes through porous membranes and human dentine, *J. Electroanal. Chem.* **1996**, *408*, 125-140.
  63. Frank, M. H. T.; Denuault, G. ; Scanning Electrochemical Microscopy - Probing the Ingress and Egress of Protons from a Polyaniline Film, *J. Electroanal. Chem.* **1993**, *354*, 331-339.
  64. Macpherson, J. V.; Unwin, P. R. ; A New Approach to the Study of Dissolution Kinetics, *J. Chem. Soc.-Faraday Trans.* **1993**, *89*, 1883-1884.
  65. Macpherson, J. V.; Unwin, P. R. ; A Novel-Approach to the Study of Dissolution Kinetics Using the Scanning Electrochemical Microscope-theory and Application to Copper-Sulfate Pentahydrate Dissolution in Aqueous Sulfuric-Acid-Solutions, *J. Phys. Chem.* **1994**, *98*, 1704-1713.

66. Macpherson, J. V.; Unwin, P. R. ; Scanning Electrochemical Microscope Induced Dissolution rate Law and Reaction-Rate Imaging for Dissolution of the (010) Face of Potassium Ferrocyanide Trihydrate in Nonstoichiometric Aqueous Solutions of the Lattice Ion., *J. Phys. Chem.* **1995**, *99*, 3338-3351.
67. Macpherson, J. V.; Unwin, P. R. ; Scanning electrochemical microscope-induced dissolution: Theory and experiment for silver chloride dissolution kinetics in aqueous solution without supporting electrolyte, *J. Phys. Chem.* **1996**, *100*, 19475-19483.
68. Macpherson, J. V.; Slevin, C. J.; Unwin, P. R. ; Probing the oxidative etching kinetics of metals with the feedback mode of the scanning electrochemical microscope, *J. Chem. Soc.-Faraday Trans.* **1996**, *92*, 3799-3805.
69. Borgwarth, K.; Ricken, C.; Ebling, D. G.; Heinze, J. ; Surface Characterization and Modification by the Scanning Electrochemical Microscope (SECM), *Ber. Bunsenges. Phys. Chem.* **1995**, *99*, 1421-1426.
70. Zhu, Y. Y.; Williams, D. E. ; Scanning electrochemical microscopic observation of a precursor state to pitting corrosion of stainless steel, *J. Electrochem. Soc.* **1997**, *144*, L43-L45.
71. Jehoulet, C.; Obeng, Y. S.; Kim, Y. T.; Zhou, F. M.; Bard, A. J. ; Electrochemistry and Langmuir Trough Studies of C-60 and C-70 Films, *J. Am. Chem. Soc.* **1992**, *114*, 4237-4247.
72. Scott, E. R.; White, H. S.; Phipps, J. B. ; Scanning Electrochemical Microscopy of a Porous Membrane, *J. Membr. Sci.* **1991**, *58*, 71-87.
73. Sugimura, H.; Uchida, T.; Kitamura, N.; Masuhara, H. ; Scanning Tunneling Microscopy Tip-Induced Anodization for Nanofabrication of Titanium, *J. Phys. Chem.* **1994**, *98*, 4352-4357.
74. Vitt, J. E.; Engstrom, R. C. ; Imaging of oxygen evolution and oxide formation using quinine fluorescence, *Anal. Chem.* **1997**, *69*, 1070-1076.

- 
75. Wei, C.; Bard, A. J.; Mirkin, M. V. ; Scanning Electrochemical Microscopy. 31. Application of SECM to the Study of Charge-Transfer Processes at the Liquid-Liquid Interface, *J. Phys. Chem.* **1995**, *99*, 16033-16042.
76. Solomon, T.; Bard, A. J. ; Scanning Electrochemical Microscopy. 30. Application of Glass Micropipet Tips and Electron-Transfer at the Interface Between 2 Immiscible Electrolyte-Solutions for SECM Imaging, *Anal. Chem.* **1995**, *67*, 2787-2790.
77. Solomon, T.; Bard, A. J. ; Reverse (Uphill) Electron-Transfer at the Liquid-Liquid Interface, *J. Phys. Chem.* **1995**, *99*, 17487-17489.
78. Selzer, Y.; Mandler, D. ; A novel approach for studying charge transfer across an interface of two immiscible solutions using the scanning electrochemical microscope (SECM), *J. Electroanal. Chem.* **1996**, *409*, 15-17.
79. Tsionsky, M.; Bard, A. J.; Mirkin, M. V. ; Scanning electrochemical microscopy. 34. Potential dependence of the electron-transfer rate and film formation at the liquid/liquid interface, *J. Phys. Chem.* **1996**, *100*, 17881-17888.
80. Slevin, C. J.; Umbers, J. A.; Atherton, J. H.; Unwin, P. R. ; A new approach to the measurement of transfer rates across immiscible liquid/liquid interfaces, *J. Chem. Soc.-Faraday Trans.* **1996**, *92*, 5177-5180.
81. Shao, Y. H.; Mirkin, M. V.; Rusling, J. F. ; Liquid/liquid interface as a model system for studying electrochemical catalysis in microemulsions. Reduction of trans-1,2-dibromocyclohexane with vitamin B-12, *J. Phys. Chem. B* **1997**, *101*, 3202-3208.
82. Tsionsky, M.; Bard, A. J.; Mirkin, M. V. ; Long-range electron transfer through a lipid monolayer at the liquid/liquid interface, *J. Am. Chem. Soc.* **1997**, *119*, 10785-10792.

83. Horrocks, B. R.; Schmidtke, D.; Heller, A.; Bard, A. J. ; Scanning Electrochemical Microscopy. 24. Enzyme Ultramicroelectrodes for the Measurement of Hydrogen-Peroxide a Surfaces, *Anal. Chem.* **1993**, *65*, 3605-3614.
84. Yamada, H.; Shiku, H.; Matsue, T.; Uchida, I. ; Microvoltammetric Characterization of Diaphorase Monolayer at Glass Surface, *Bioelectrochem. Bioenerg.* **1994**, *33*, 91-93.
85. Grundig, B.; Wittstock, G.; Rudel, U.; Strehlitz, B. ; Mediator-Modified Electrodes for Electroanalytic Oxidation of NADH, *J. Electroanal. Chem.* **1995**, *395*, 143-157.
86. Wittstock, G.; Yu, K. J.; Halsall, H. B.; Ridgway, T. H.; Heineman, W. R. ; Imaging Immobilized Antibody Layers with Scanning Electrochemical Microscopy, *Anal. Chem.* **1995**, *67*, 3578-3582.
87. Shiku, H.; Matsue, T.; Uchida, I. ; Detection of microspotted carcinoembryonic antigen on a glass substrate by scanning electrochemical microscopy, *Anal. Chem.* **1996**, *68*, 1276-1278.
88. Gilbert, J. L.; Smith, S. M.; Lautenschlager, E. P. ; Scanning Electrochemical Microscopy of Metallic Biometals - Reaction-Rate and Ion Release Imaging Modes, *J. Biomed. Mater. Res.* **1993**, *27*, 1357-1366.
89. Kranz, C.; Lotzbeyer, T.; Schmidt, H. L.; Schuhmann, W. ; Lateral visualization of direct electron transfer between microperoxidase and electrodes by means of scanning electrochemical microscopy, *Biosens. Bioelectron.* **1997**, *12*, 257-266.
90. Kranz, C.; Wittstock, G.; Wohlschlager, H.; Schuhmann, W. ; Imaging of microstructured biochemically active surfaces by means of scanning electrochemical microscopy, *Electrochim. Acta* **1997**, *42*, 3105-3111.
91. Lee, C.; Kwak, J. Y.; Bard, A. J. ; Application of Scanning Electrochemical Microscopy to Biological Samples, *Proc. Natl. Acad. Sci. U. S. A.* **1990**, *87*, 1740-1743.

92. Jackson, R. B.; Tsionsky, M.; Cardon, Z. G.; Bard, A. J. ; Guard cell photosynthesis as measured with a new scanning electrochemical microscope, *Plant Physiol.* **1996**, *111*, 354-354.
93. Tsionsky, M.; Cardon, Z. G.; Bard, A. J.; Jackson, R. B. ; Photosynthetic electron transport in single guard cells as measured by scanning electrochemical microscopy, *Plant Physiol.* **1997**, *113*, 895-901.
94. Pierce, D. T.; Bard, A. J. ; Scanning Electrochemical Microscopy. 23. Reaction Localization of Artificially Patterned and Tissue-Bond Enzymes, *Anal. Chem.* **1993**, *65*, 3598-3604.
95. Zhou, J. F.; Wipf, D. O. ; Deposition of conducting polyaniline patterns with the scanning electrochemical microscope, *J. Electrochem. Soc.* **1997**, *144*, 1202-1207.

## **Part II**

# **Implementation and Experiments**





This part will cover the implementation of the nanotools introduced in the previous part. In the first chapter the fabrication of a special sample holder for AFM patch clamp experiments and a particular conductive AFM probe for local electrochemical experiments will be addressed. I'd like to mention here that the design and microfabrication of the AFM probes were realized by Dr. T. Akiyama. A detailed fabrication process for both tools is presented in the Appendix. The second chapter will deal with the experiments conducted with the microfabricated tools. In particular the chapter will focus on combined SECM-AFM experiments.



## **Chapter 2**

# **Fabrication**

## 2.1 Towards a Planar Sample Support for in-situ Experiments in Structural Biology <sup>a</sup>

This section reports about the development of a planar support for biological samples. Its aim is to combine AFM and patch clamp measurements, in order to simultaneously acquire topography and electrical properties of biological membranes. The fabrication of Sub-micrometer apertures using standard MEMS techniques and the assessment of the electrical quality of the support are presented.

### 2.1.1 Introduction

Channel proteins that are embedded in cell membranes, are responsible for several elementary cell functions. Consequently, there is a great interest in understanding the working principle of these channels. The patch clamp technique can give insight in the electrical behavior of such proteins.<sup>1</sup> In method a glass pipette is used to aspirate a patch of a cell membrane. A pair of electrodes are positioned across the membrane, such that an ion current can be measured as function of the applied voltage. Atomic force microscopy (AFM), has excessively been applied to measure the topography of membranes and to monitor topographical changes as function of pH or globally applied electrical potentials.<sup>2,3</sup> In order to learn more about the correlation between the structure and the functionality of membrane channels, it is advantageous to simultaneously observe the electrical and topographic information. This could be achieved by means of a setup that combines conventional patch-clamp technique and AFM.<sup>4,5</sup> However, it is difficult to operating an AFM at the apex of a pipette tip. This problem can be solved by a planar sample support featuring a micro metric aperture, which allows accessing the adsorbed membrane from both sides. Figure 2.1 shows the schematic representation of the proposed setup. The biological membrane is adsorbed onto a thin  $Si_xN_y$  film, featuring a sub micron sized aperture.

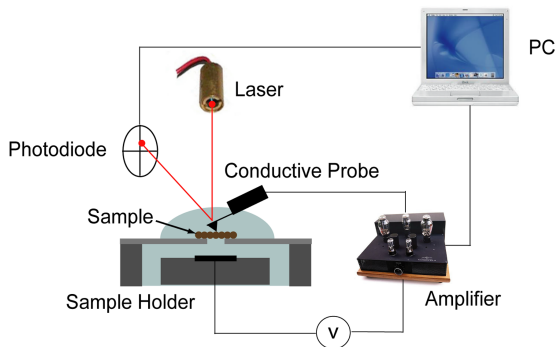
---

<sup>a</sup>This section was the base for a publication submitted to Microelectronic Eng.: M. R. Gullo, T. Akiyama, P.L.T.M. Frederix, A. Tonin, U. Staufer, A. Engel, N. F. de Rooij, Microelectronic Eng., 78-79, 571-574 .

One electrode is embedded in the micro channel beneath the aperture and the  $Si_xN_y$  membrane; the counter electrode is implemented into a conductive AFM probe.<sup>6</sup> By applying an electric potential between these two electrodes it is possible to acquire the electrical characteristic of the biological membrane.

## 2.1.2 Fabrication

The difficulty in the fabrication of a planar patch clamp supports for biological applications is the tight, giga ohm seal needed between the biological membrane and the support.<sup>7-9</sup> In most planar supports the sample is only laid onto the surface, compared to patch clamping, where the membrane is partially sucked into the aperture and hence, uniformly covers a large surface. We therefore assume that the surface roughness of the planar support plays a great role for achieving a good seal. AFM measurements of  $Si_xN_y$  films deposited onto bare Si, showed a roughness of  $5nm$  rms. However, using the contact side of the interface that is accessible after removing the Si, improved that value to  $0.12nm$  rms (figure 2.2). Low values of RC noise

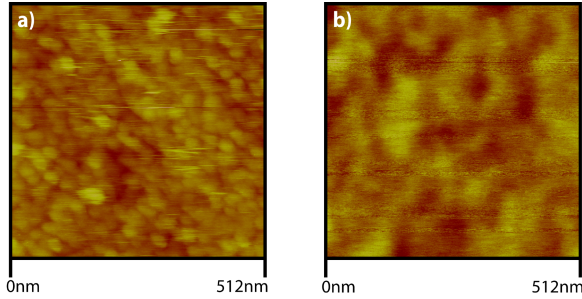


**Figure 2.1:** Schematic representation of the setup. The biological membrane is adsorbed onto the patch-clamp support. One electrode is embedded in the micro channel beneath the aperture; the counter electrode is implemented into conductive AFM probe.

are crucial for obtaining highly accurate single channel recordings. Noise of parasitic capacitances can easily mask the current generated by a single ion channel.<sup>10</sup> Therefore, keeping the parasitic capacitance and series resistance of the supports low is important for single channel recordings. To fabricate our sample supports we used a two-mask process: A  $Si_xN_y$  film was deposited onto a Si (100) wafer by low-pressure chemical vapor deposition (LPCVD). Micron sized holes were structured into the  $Si_xN_y$  film by standard photo lithography and reactive ion etching (RIE) (figure 2.3a). The patterned  $Si_xN_y$  film was then released by KOH. The holes in the freestanding  $Si_xN_y$  membrane were shrunk to sub micron-size by a second  $Si_xN_y$  LPCVD deposition (figure 2.3b). Alternatively, before releasing the  $Si_xN_y$  membrane a blanked RIE followed a by second  $Si_xN_y$  LPCVD deposition, formed an annular inlay in the aperture, which reduced the aperture diameter as well (figure 2.3c). The optimum diameter for biological membranes patches varies depending on the particular application and the size of the biological sample it self. Biological membrane patches such as Bacteriorhodopsin have generally diameters of  $1\mu m$ . Thus aperture diameters are  $0.1\mu m$  to  $0.5\mu m$  are usable. The batch fabrication process presented in this section was designed in order to fabricated apertures in this size range, without changing the mask set just by simply varying the thickness of the second LPCVD deposited  $Si_xN_y$  film. The wafer was then anodically bonded onto a pyrex wafer, featuring trough holes connected by a micro channel that provides access to the backside of the biological sample. This channel was manufactured by lithography and etched in 20% HF.

### 2.1.3 Experiments

The additional parasitic capacitance of the system for patch clamp recordings should preferably be less than the capacitance of the membrane patch, such that the membrane is dominant.<sup>11</sup> In order to extract the series resistance and capacitance of the supports, a phase gain analyzer with Ag/AgCl electrodes was used. The samples were placed in a testing apparatus and electrically isolated. The micro channel and the front side of the support were filled with  $50mM$  KCl electrolyte solution. The Ag/AgCl electrodes were

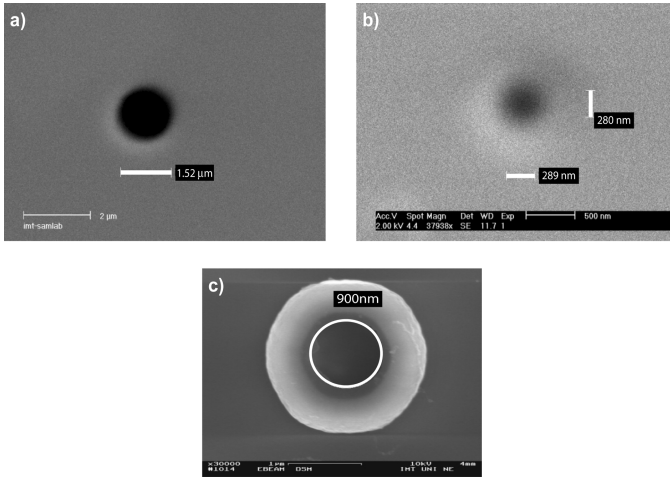


**Figure 2.2:** a) AFM measurement of the front side surface of the  $Si_xN_y$  membrane. The z-range is  $6nm$  and the rms roughness is  $5nm$ . b) AFM image of the released backside surface of the  $Si_xN_y$  membrane. The z-range is  $1.2nm$  and the rms roughness has improved to  $0.113nm$ .

then immersed into the liquid from both sides of the membrane. The impedance spectra were acquired by using a 200 mV excitation voltage with a 1 Hz to 1 kHz frequency sweep. The equivalent circuit used to model the impedance spectra is a resistance and a capacitor connected in parallel. The measured impedance spectra were then fitted to the model in order to obtain the resistance of the aperture and the support capacitance. The overall system resistance is dominated by the conductance of the aperture due to its small dimension compared to the rest of the conducting path. Therefore, the systems resistance can be acceptably modeled by only taking into account the resistance of the aperture. The later can be modeled as a conductor with a resistivity matching that of the KCl solution.<sup>12</sup> The resistances of supports with three different aperture radii were measured. The results presented in figure 2.4 shows good agreement between the calculated resistance and the measured aperture resistance. The capacitance of the support is generated by the conducting parallel plates of KCl solution separated by the  $Si_xN_y$  dielectric and is given by

$$C = \frac{\epsilon_r \epsilon_0 A}{d} \quad (2.1)$$

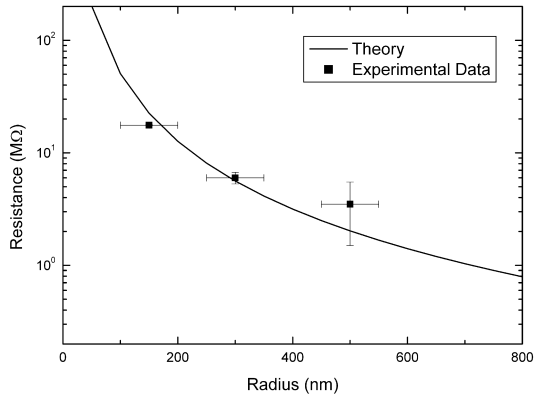
where C is the capacitance,  $\epsilon_r$  is the relative permeability of the  $Si_xN_y$ ,  $\epsilon_0$  is the vacuum permeability,  $d$  the thickness of the  $Si_xN_y$  membrane ( $1.2\mu m$ )



**Figure 2.3:** a) SEM image of the aperture in the freestanding  $Si_xN_y$  film realized by photo lithography and RIE. The diameter of the aperture is  $1.5\mu m$ . b) The same aperture after a deposition of  $650nm$  of  $Si_xN_y$  by low-pressure chemical vapor deposition (LPCVD). The diameter of the aperture has shrunken to  $290nm$ . c) SEM image of an aperture after a second LPCVD of  $600nm$   $Si_xN_y$  and a blank RIE before releasing the  $Si_xN_y$  membrane. The annular inlet reduced the aperture diameter by  $1\mu m$ .

and  $A$  is the area of the suspended  $Si_xN_y$  membrane ( $3.1mm^2$ ). This model overestimates the capacitance, as there will be an additional straight capacitance from the non-suspended portion  $Si_xN_y$  membrane. This additional capacitance is in parallel with our model capacitance and should thus increase the overall capacitance. The capacitances of supports with three different aperture radii were acquired. 5 devices were measured for each hole size and the resulting mean capacitance was  $167pF$  with a variation of  $63pF$ . The measured capacitance shows a reasonable agreement with the calculated capacitance ( $191pF$ ). The high variation in the experimental value results from the different size of the micro channel and, hence, the different areas of fluid contact.





**Figure 2.4:** Measurement of the ionic resistance through the aperture vs. the radius of the aperture. The line represents the theoretical values and the points represent the values measured for the three different hole sizes. The apertures with the radii  $150\text{nm}$ ,  $300\text{nm}$  and  $500\text{nm}$  showed an ionic resistance of  $3.5\text{M}\Omega$ ,  $6\text{M}\Omega$  and  $17.6\text{M}\Omega$  respectively.

## 2.1.4 Conclusion

A planar sample support for combining patch clamp and AFM measurements on biological membranes was developed and fabricated. The capacitance of the supports need to be smaller than the capacitance of the biological membrane confined by the aperture in order to make single channel detection possible. The capacitance of a membrane patch is about  $1.3\mu\text{F}/\text{cm}^2$  (Ref.<sup>10</sup>). The corresponding capacitances for biological membrane patches with an area corresponding to our three different aperture radii ( $150\text{nm}$ ,  $300\text{nm}$ ,  $500\text{nm}$ ) are  $0.9\text{fF}$ ,  $3.7\text{fF}$  and  $10\text{fF}$  respectively. The current device will therefore hardly allow single channel measurements. Increasing the  $\text{Si}_x\text{N}_y$  membrane thickness and reducing the surface of the membrane exposed to the liquid could mitigate these effects. Nevertheless, it will be possible to visualize conformational changes of the membrane protein channels with the present device.

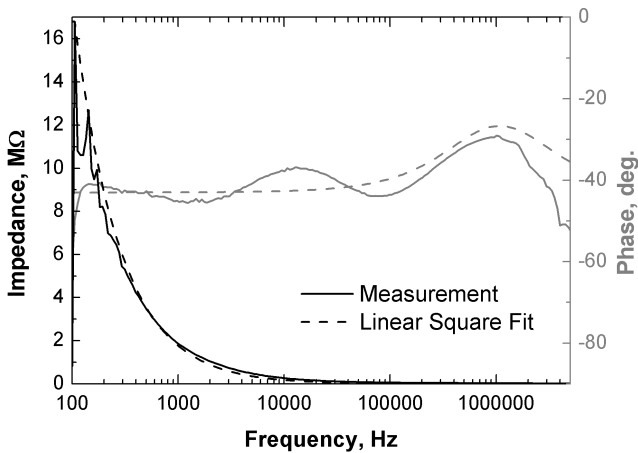
## Bibliography

1. Ypey, D. L.; DeFelice, L. J. *The Patch-Clamp Technique*; Vanderbilt University Medical Center Press: Vanderbilt, 1999.
2. Engel, A.; Mueller, D. ; Observing single biomolecules at work with the atomic force microscope, *Nat. Struct. Biol.* **2000**, *7*, 715-718.
3. Scheuring, S.; Fotiadis, D.; Moeller, C.; Mueller, S. A.; Engel, A.; Mueller, D. J. ; Single proteins observed by atomic force microscopy, *Single Mol.* **2001**, *2*, 59-67.
4. Mosbacher, J.; Haeberle, W.; Hoerber, J. ; Studying membranes with scanning force microscopy and patch-clamp technique, *J. Vac. Sci. Technol. B* **1996**, *14*, 1449-1452.
5. Langer, M.; Oeffner, W.; Wittmann, H.; Floesser, H.; Schaar, H.; Haeberle, W.; Pralle, A.; Ruppertsberg, J.; Hoerber, J. ; A scanning force microscope for simultaneous force and patch-clamp measurements on living cell tissues, *Rev. Sci. Instrum.* **1997**, *68*, 2583-2590.
6. Akiyama, T.; Gullo, M. R.; de Rooij, N. F.; Tonin, A.; Hidber, H. R.; Frederix, P. L. T. M.; Engel, A.; Staufer, U. ; Development of insulated conductive probes with platinum silicide tips for atomic force microscopy in cell biology, *Japan. J. Appl. Phys. Part 1-Regular Papers Short Notes & Review Papers* **2004**, *43*, 3865-3867.
7. Fertig, N.; Tilke, A.; Blick, R.; Kotthaus, J.; Behrends, J. C.; ten Bruggencate, G. ; Stable integration of isolated cell membrane patches in a nanomachined aperture, *Appl. Phys. Lett.* **2000**, *77*, 1218-1220.
8. Fertig, N.; Blick, R. H.; Behrends, J. C. ; Whole cell patch clamp recording performed on a planar glass chip, *Biophys. J.* **2002**, *82*, 3056-3062.
9. Fertig, N.; Klau, M.; George, M.; Blick, R. H.; Behrends, J. C. ; Activity of single ion channel proteins detected with a planar microstructure, *Appl. Phys. Lett.* **2002**, *81*, 4865-4867.

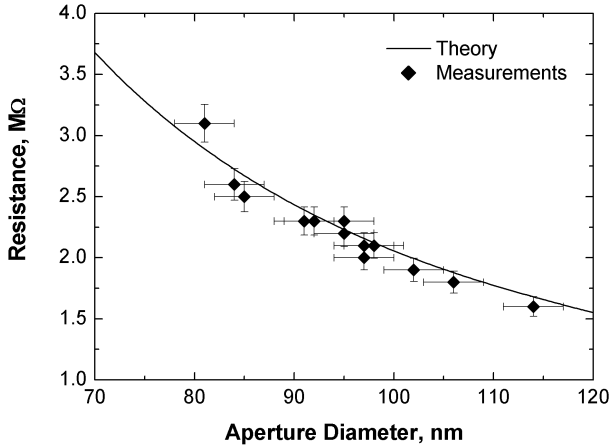
10. Sakmann, B.; Neher, E. *Single-Channel Recording*; Plenum Press: New York, NY, 1983.
11. Thompson, R. E.; Lindau, M.; Webb, W. W. ; Robust, high-resolution, whole cell patch-clamp capacitance measurements using square wave stimulation, *Biophys. J.* **2001**, *81*, 937-948.
12. Macpherson, J. V.; Jones, C. E.; Barker, A. L.; Unwin, P. R. ; Electrochemical imaging of diffusion through single nanoscale pores, *Anal. Chem.* **2002**, *74*, 1841-1848.

## 2.2 Latest Results for the Sample Support

The planar sample support chip had to be redesigned in order to improve the issues addressed in the previous section. The objectives were to further reduce the aperture size and to decrease the capacitance of the support. The first issue was solved by structuring the aperture by means of e-beam lithography and RIE. In order to have an optimal aperture size without increasing the resistance of the current flowing through it, a size of 100nm was selected. A reduction of the capacity was achieved by reducing the area of the freestanding membrane and by increasing its thickness with an additional silicon oxide layer. For a detailed fabrication process flow please refer to the appendix. The mentioned criteria of new planar support chips were investigated with the same setup and fitting method described in the previous section. Figure 2.5 shows the resulting phase/gain plot and the fit to the electric model corresponding to the planar sample support. Based on the fit of the respective chips it was possible to determine the resistance



**Figure 2.5:** Phase/gain plot of the planar sample support in 1M KCl. The dotted lines show the linear-square fit of the phase/gain plot.

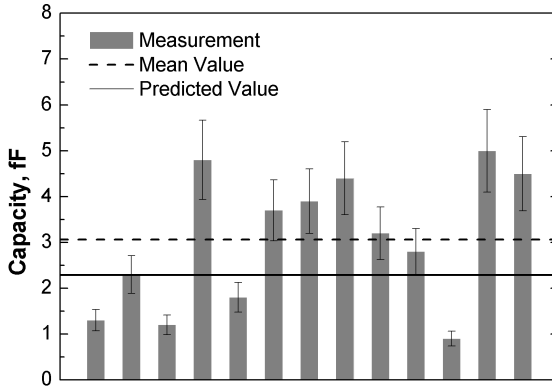


**Figure 2.6:** Resistances of the aperture, determined by the linear-square fit of the phase/gain plot. The line represents the theoretical resistance in function of the aperture diameter for 1M KCl.

of their aperture (figure 2.6). The theoretical curve was calculated with the following equation<sup>1</sup>

$$R = 4 \frac{(l + 0.8d)}{\pi k d^2}, \quad (2.2)$$

where  $l$  is the aperture depth (100nm),  $k$  the conductivity of the electrolyte (measured previously to the experiment:  $1.12 \cdot 10^{-8} \text{ 1}/\Omega\text{nm}$  for 1M KCl) and  $d$  the aperture diameter. The measured resistances correlate with the theoretical value and confirm the accuracy of the fitting model. Compared to the previous planar sample support chip, the resistances are 100 times smaller. This is due to the local thinning of the suspended membrane (down to 100nm) and thus to a less deep aperture. This was necessary to enable the e-beam patterning and RIE to etch through the membrane (see appendix). The otherwise thicker membrane and its reduced area compared to the previous chip design allowed to drastically decrease the membrane capacitance. Figure 2.7 shows the capacitances deduced from the fit



**Figure 2.7:** Capacitance of the new planar sample support chips derived from the fitting of the respective phage gain plot. The dotted line indicates the mean capacitance of 3fF and the straight line shows the predicted value based on the design of the chip.

of the respective phase gain plots. Even if the mean capacitance (3fF) is above the predicted capacitance (2.3fF) it fulfills the requirements for single channel recording described in the previous section. First experiments with biological samples will be shown later.

## **Bibliography**

1. Ito, T.; Sun, L.; Crooks, R. M. ; Simultaneous determination of the size and surface charge of individual nanoparticles using a carbon nanotube-based coulter counter, *Anal. Chem.* **2003**, *75*, 2399-2406.

## 2.3 Insulated conductive probes for in situ experiments in cell biology<sup>b</sup>

This section reports about the development of a multifunctional AFM probe, which allows to perform simultaneous measurements of topography and electrical properties of biological samples in a buffer solution. The quality of the AFM probes has been experimentally assessed: Topography and electric current images of HOPG in buffer solution and topography measurements of bacteriorhodopsin membranes in buffer solution.

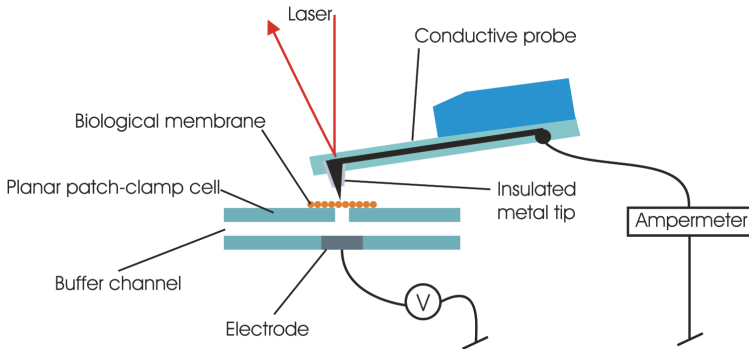
### 2.3.1 Introduction

Channel proteins, which are embedded in cell membranes, are responsible for a variety of elementary cell functions, e.g. nutrient or ion transport. Consequently, there is a great interest in understanding the transport mechanism through these channels. The patch clamp technique gives insight in the electrical behavior of the proteins.<sup>1</sup> This method generally uses a glass pipette to mount a cell membranes and an electrode pair positioned across the membrane to measure the ion current across the membrane at different applied voltages. With the patch-clamp technique the conductance through the membrane can be measured, ranging from the conductance of a whole cell to estimate the number of channels down to the single channel conductance to determine its opening and closing characteristics.<sup>1</sup> Atomic force microscopy (AFM) has been applied to measure the topography of membranes and monitor changes at the surface of active membrane proteins, with sub-nanometer lateral resolution.<sup>2,3</sup> Because samples in the atomic force microscope can be operated in fluid the proteins can be monitored in a native environment. To learn more about the structure-function relationship of membrane channels it would be advantageous to observe the electrical and topographic information simultaneously. This can be done

---

<sup>b</sup>This section was the base for a publication submitted to Scanning Tunneling Microscopy/Spectroscopy and Related Techniques: M. R. Gullo, T. Akiyama, P.L.T.M. Frederix, A. Tonin, U. Stauffer, A. Engel, N.F. de Rooij, Scanning Tunneling Microscopy/Spectroscopy and Related Techniques, American Institute of Physics, 166-171.



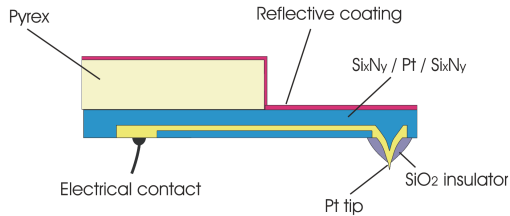


**Figure 2.8:** Experimental setup.

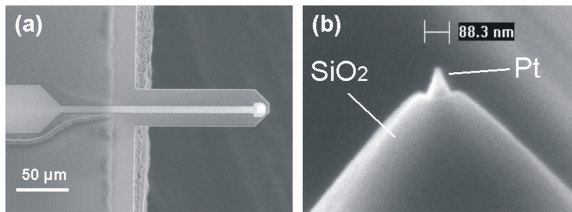
using a setup that combines the conventional patch-clamp technique and AFM.<sup>4,5</sup> However, the application of scanning probe techniques over the end of the patch-clamp pipette is technically demanding, due to the pipette geometry. This problem can be overcome by using a planar patch clamp support.<sup>6</sup> Figure 2.8 shows a schematic representation of a setup that uses a planar patch clamp support for combined electrical and topographic measurements. One electrode is embedded in the support, under the membrane. To enable the sensing of local variations in the electrical properties over the membrane, the counter electrode is implemented in the cantilever. This section will focus on the fabrication and characterization of the conductive cantilever.

### 2.3.2 Probe Design

The challenge in fabricating conducting probes for biological applications is to keep the characteristics of the mechanical part, (spring constant, resonance frequency and tip radius) as close as possible to the currently available silicon-nitride ( $\text{Si}_3\text{N}_4$ ) cantilevers. Furthermore, the exposed materials must be biocompatible and the cantilever must be operable in buffer solution. To avoid leakage currents through the buffer solution, the tip and the lead must be electrically insulated from the buffer solution by a dielectric film except

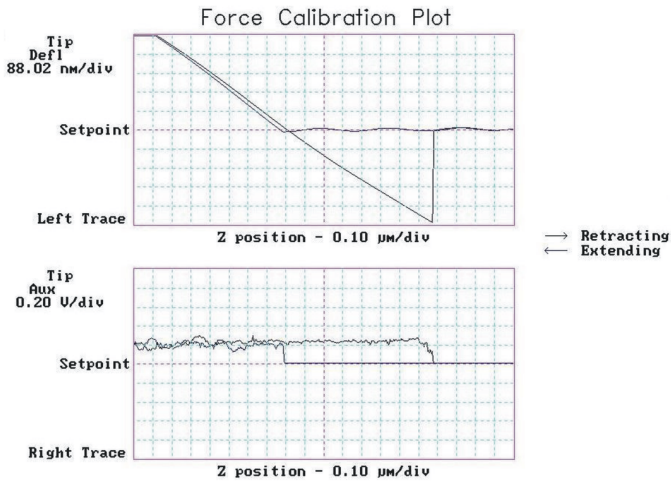


**Figure 2.9:** Schematic representation of the conductive AFM probe.



**Figure 2.10:** Silicon-nitride cantilever probes with embedded electrical lead from a contact pad to the metal (platinum) tip. b) The tip diameter is about  $15\text{nm}$  and the exposed height amounts to  $90\text{nm}$ .

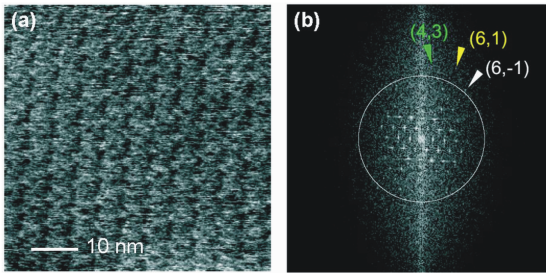
at the very apex of the tip. Kueng et al. have recently reported about gold-coated  $\text{Si}_3\text{N}_4$ -cantilevers, which were insulated by a vapor deposited polymer (parylene).<sup>7</sup> They opened the parylene coating at the apex by means of a focused ion beam. This formed a square-frame shaped electrode of a side-length of about  $800\text{nm}$  at about  $300\text{nm}$  behind the tip apex. This probe might be used for our application. However, more local measurement of the electronic properties would be desirable. Therefore only the tip-apex itself should be conductive. The here presented conductive probe (see Fig. 2.9) shows a metal electrode embedded in an electrically insulating  $\text{Si}_3\text{N}_4$  layer. The tip is shielded by silicon-oxide. Only the very apex of the tip is electrically conducting. The electrical connection can be established by a contact pad located on the handling chip.



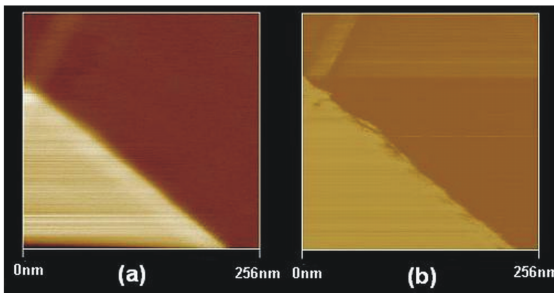
**Figure 2.11:** Approach curve to an HOPG surface in air, the upper graph shows the deflection signal and the lower image shows the current signal.

### 2.3.3 Fabrication

The following full wafer batch process was developed. A Si(100) wafer was oxidized and a  $\text{Si}_3\text{N}_4$  film was deposited by a low pressure chemical vapor deposition (LPCVD) process. Squares were then opened in it by photolithography and reactive ion etching (RIE), exposing the underlying Si surface. Etching the wafer in KOH was carried out to form a pyramidal mold. A thermal wet-oxidation step at  $950^\circ\text{C}$ , called oxide-sharpening, was then performed to narrow the pit. Electrodes consisting of Ta  $5\text{nm}$  / Pt  $130\text{nm}$  were delineated by means of the lift-off technique. A second LPCVD  $\text{Si}_3\text{N}_4$  film was deposited to completely encapsulate the metal. The two nitride films were then etched at the same time to define the cantilever shape. As in the case of standard  $\text{Si}_3\text{N}_4$  cantilevers, pyrex-chips are anodically bonded to the nitride, which will be used as handling chips. After the bonding, the Si is completely removed in KOH and the oxide around the tip was opened at the apex by means of a timed etch in buffered HF. Finally a reflective coating



**Figure 2.12:** a) AFM topography image of the intracellular side of Bacteriorhodopsin, imaged with a conductive tip in buffer solution (Z range:  $0.88\text{nm}$ ,  $128\text{nm} \times 128\text{nm}$  rectangle). b) FFT spectrum of image. Circle:  $1\text{nm}$  resolution; arrow heads: Diffraction spots:  $(4,3) = 0.88\text{nm}$   $(6,1) = 0.82\text{nm}$   $(6,-1) = 0.96\text{nm}$ .



**Figure 2.13:** Simultaneous measurement of (a) topography (Z range:  $8\text{nm}$ ) and (b) electrical current (Z range:  $10\mu\text{A}$ ) of HOPG in buffer solution.

is evaporated on the top side of the probe.

### 2.3.4 Experiments

The mechanical characteristics of the probe were investigated. The cantilevers have a spring constant of typical  $0.1\text{N/m}$  and a resonance frequency around  $15\text{kHz}$ . These values are comparable to the conventional  $\text{Si}_3\text{N}_4$ -cantilevers. SEM photographs (see Fig. 2.10) showed that tip radii below  $8\text{nm}$  have been routinely achieved. Several AFM experiments have been performed to investigate the imaging quality and the conductivity of the metal

tip. All the measurements have been performed with a commercial AFM. Figure 2.11 shows an approach curve of the conductive probe to a HOPG surface in air. It can be seen that an electrical contact was established when the tip came into contact with the surface. During retracting, the electric contact was lost when the tip snaps out from the HOPG surface. The same measurements were performed in deionized water and buffer solution with a pH of 7.8. All measurements showed similar curves as in Fig. 2.11. Figure 2.12 shows an AFM image of bacteriorhodopsin (purple membrane) recorded in buffer solution. The buffer solution was optimized for having sharper images<sup>8</sup> and consists of 20mM Tris-HCl, 150mM KCl, 25mM MgCl<sub>2</sub>. A sufficient resolution below 1nm for imaging biological membranes was achieved. The single proteins can be observed. Figure 2.13 shows a simultaneously recorded topography and electrical current image of HOPG in buffer solution. It can be seen from this image that the topography correlates to the conductance image. The higher plateau shows a higher conductance.

### **2.3.5 Conclusion**

The fabrication of a conductive probe, which is electrically insulated except at the very apex of the tip has been presented. It has been shown that the mechanical characteristics and the sharpness of the platinum tip sufficed to obtain subnanometer lateral resolution on a biological sample in buffer solution. Conductance images recorded in buffer solutions showed the capability to measure local current variations with a few nanometer spatial resolution and that a good correlation existed with the in parallel recorded topography.

## Bibliography

1. Ypey, D. L.; DeFelice, L. J. *The Patch-Clamp Technique*; Vanderbilt University Medical Center Press: Vanderbilt, 1999.
2. Engel, A.; Mueller, D. ; Observing single biomolecules at work with the atomic force microscope, *Nat. Struct. Biol.* **2000**, *7*, 715-718.
3. Scheuring, S.; Fotiadis, D.; Moeller, C.; Mueller, S. A.; Engel, A.; Mueller, D. J. ; Single proteins observed by atomic force microscopy, *Single Mol.* **2001**, *2*, 59-67.
4. Mosbacher, J.; Haeberle, W.; Hoerber, J. ; Studying membranes with scanning force microscopy and patch-clamp technique, *J. Vac. Sci. Technol. B* **1996**, *14*, 1449-1452.
5. Langer, M.; Oeffner, W.; Wittmann, H.; Floesser, H.; Schaar, H.; Haeberle, W.; Pralle, A.; Ruppertsberg, J.; Hoerber, J. ; A scanning force microscope for simultaneous force and patch-clamp measurements on living cell tissues, *Rev. Sci. Instrum.* **1997**, *68*, 2583-2590.
6. Fertig, N.; Tilke, A.; Blick, R.; Kotthaus, J.; Behrends, J. C.; ten Brug-gencate, G. ; Stable integration of isolated cell membrane patches in a nanomachined aperture, *Appl. Phys. Lett.* **2000**, *77*, 1218-1220.
7. Kueng, A.; Kranz, C.; Mizaikoff, B.; Lugstein, A.; Bertagnolli, E. ; Combined scanning electrochemical atomic force microscopy for tapping mode imaging, *Appl. Phys. Lett.* **2003**, *82*, 1592-1594.
8. Mueller, D. J.; Fotiadis, D.; Scheuring, S.; Mueller, S. A.; Engel, A. ; Electrostatically balanced subnanometer imaging of biological specimens by atomic force microscope, *Biophys. J.* **1999**, *76*, 1101-1111.

## **Chapter 3**

# **Experiments**

## 3.1 Microfabricated Probes for Combined Atomic Force and Scanning Electrochemical Microscopy<sup>a</sup>

This section will present a combined atomic force and scanning electrochemical microscope (AFM-SECM) probe. The probe is electrically insulated except at the tip apex, which has a radius of curvature of 10-15nm. Steady-state cyclic voltammetry and feedback experiments for the reduction of  $\text{Ru}(\text{NH}_3)_6\text{Cl}_3$ , showed a distinct and reproducible response of the electrode. These experimental results agreed well with the finite element simulations for the corresponding diffusion process. Sequentially topographical and electrochemical studies of microfabricated Pt lines spaced 100nm apart (edge to edge) and deposited on  $\text{Si}_3\text{N}_4$  showed a lateral electrochemical image resolution of 10 nm.

### 3.1.1 Introduction

Scanning Electrochemical Microscopy (SECM), is part of the scanning probe microscopy (SPM) family. In SECM, ultra microelectrodes (UME) with a diameter of less than  $10\mu\text{m}$ , are used to perform in situ electrochemical experiments. The implementation of this method has been demonstrated for several applications.<sup>1-26</sup> The achievable spatial resolution strongly depends on the shape and size of the UME<sup>10</sup> as well as on the distance between UME and sample.<sup>2</sup> A way to reduce the size of the electrodes and thus improve the resolution is to microfabricate the UMEs. Furthermore by microfabrication it is possible to combine SECM with other SPM techniques, such as Atomic Force Microscopy<sup>27</sup> (AFM) or Scanning Nearfield Optical Microscopy (SNOM). This would help to simultaneously obtain complementary information.<sup>28</sup> In particular, combining SECM and AFM offers the possibility to correlate chemical surface activity with topography. The AFM allows probing the surface topography with relative low forces ( $< 1$  nN), preventing dam-

---

<sup>a</sup>This section was the base for a publication submitted to Analytical Chemistry: M. R. Gullo, P. L. T. M. Frederix, T. Akiyama, A. Engel, N. F. deRooij and U. Stauer, Characterization of Microfabricated Probes for Combined Atomic Force Microscopy and High-Resolution Scanning Electrochemical Microscopy, *Anal. Chem.*, 78, 5436-5442.

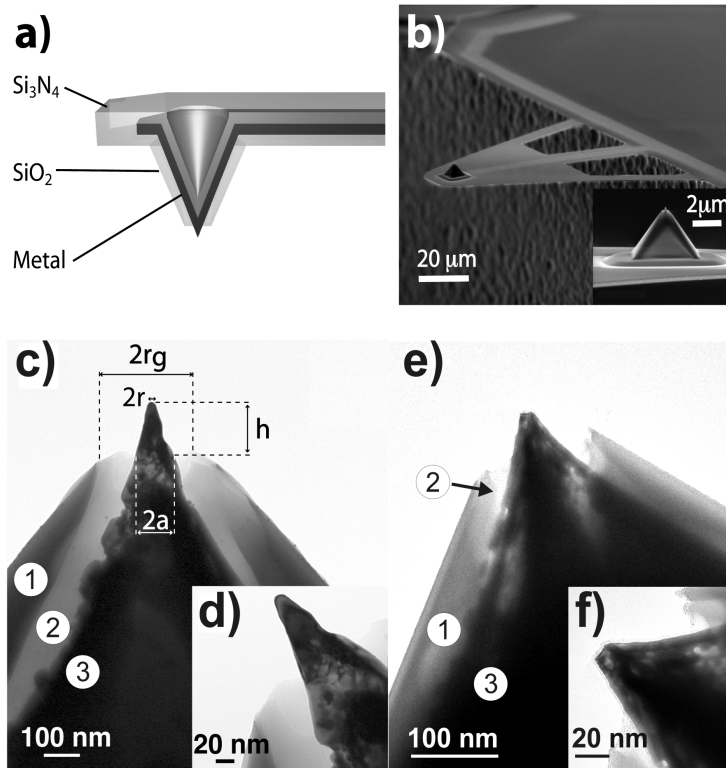


age to probe or sample, which is crucial e.g. for imaging biological material.<sup>14</sup> Moreover, the probe to sample distance can be controlled more accurately by measuring the cantilever deflection. Several fabrication strategies for such probes have already been reported. These probes proved to be functional, and combined AFM and SECM images could be recorded.<sup>6,29–39</sup> However, the achievable resolution which is related to tip sharpness and size of the electrochemically active site is still of concern in these applications. The following section presents the electrochemical characterization of batch microfabricated AFM-SECM probes, which are electrically insulated except at the tip apex (figure 3.1). The conically shaped  $\text{Pt}_x\text{Si}_y$  metal tip electrode exposed to the electrolyte featured a base width of  $\sim 100\text{nm}$ , a tip radius of curvature between  $10\text{nm}$  and  $15\text{nm}$ . The cantilever had a spring constant of  $< 0.1\text{N/m}$  (Ref.<sup>14</sup>). The fabrication process has been described in more detail in publications.<sup>40,41</sup> Finite element simulations of the diffusion limited currents, resulting from the diffusive mass transport towards the metal electrode, agreed to the corresponding measurements for  $\text{Ru}(\text{NH}_3)_6\text{Cl}_3$  in aqueous solution and supporting electrolyte. Simultaneous topographical and electrochemical imaging studies proved a clear correlation between the surface structure and its electrochemical activity: the electrochemical image showed a lateral resolution of  $10\text{nm}$ .

### 3.1.2 Experimental Setup and Finite Element Model

#### Brief Introduction to the Fabrication Process of the AFM-SECM Probes

Figure 3.1a shows a schematic representation of the conductive AFM-SECM probe. The fabrication process of this probe is based on a molding technique and is described in more detail in Appendix B. Figures 3.1c-3.1f show transmission electron microscope (TEM) micrographs of two fabricated  $\text{Pt}_x\text{Si}_y$  probe tips. The  $\text{SiO}_2$  insulation (zone 1) and the metal (zone 3) tip are clearly discernable. A gap (zone 2) between the insulation and the metal tip can be observed at the end of both tips. The gap in figure 3.1e is much smaller compared to the gap in figure 3.1c. This gap is due to a preferential etching of BHF along the metal/ $\text{SiO}_2$  interface. The geometrical values



**Figure 3.1:** a) Schematic representation of the conductive probe: The metal is embedded between two  $\text{Si}_3\text{N}_4$  thin films and the tip is insulated by  $\text{SiO}_2$ . b) Scanning electron micrograph of the fabricated probes, the height of the tip is  $5 \mu\text{m}$ . c) TEM image of the  $\text{Pt}_x\text{Si}_y$  tip apex. The contrast in zone 1 and 2 arises from the  $\text{SiO}_2$ -shell, which forms a gap to the  $\text{Pt}_x\text{Si}_y$  tip. The difference between zone 1 and 2 reflects the different amount of material that has to be transmitted when imaging at the border or across the hollow part; the contrast from the  $\text{Pt}_x\text{Si}_y$  tip is in zone 3. d) Close-up view of the tip. e) Like c) but of a tip with a much smaller gap between the insulation and the metal. f) Close-up of e).

---

	Tip 1	Tip 2	Tip 3	Tip 4
CV	(Fig. 3.4a)	(Fig. 3.4b)	(Fig. 3.4c)	(Fig. 3.5)
AC	(Fig. 3.7b)		(Fig. 3.7a)	(Fig. 3.8)
TEM	(Fig. 3.1e)			(Fig. 3.1c)
$H$	1.5	2.5	3	2
$RG$	2.6	2.3	2.2	2.3
$r$ (nm)	9	10	12	10
$a$ (nm)	21	55	105	50
$a_{CV}$ (nm)	10	40	112	45
$I_{T,\infty}$ (pA)	14	71	221	73
$I_{T,\infty}^{theory}$ (pA)	29	98	208	81
$Ca$ (pF)	25	30	75	80

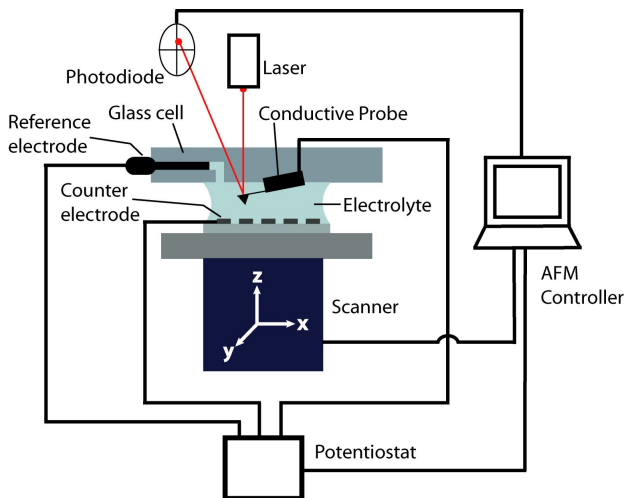
---

**Table 3.1:** The presented parameters of the tips are deduced from the corresponding TEM images. CV, AC and TEM reference the corresponding figures for the measured CV, Approach curve and TEM image respectively.  $H$  is the tip height aspect ratio,  $RG$  the insulation aspect ratio,  $r$  is tip radius of curvature,  $a$  the tip base radius at the point where the metal tip is no more surrounded by the insulating shield,  $a_{CV}$  the tip base radius calculated from CVs.  $I_{T,\infty}$  is the measured diffusion current and  $I_{T,\infty}^{theory}$  the calculated diffusion current using equation 3.7 with constants from table 3.2 and corrected according to the text.  $Ca$  is the probe capacitance,

for the tips have been deduced from these or similar TEM images and are presented in table 3.1.

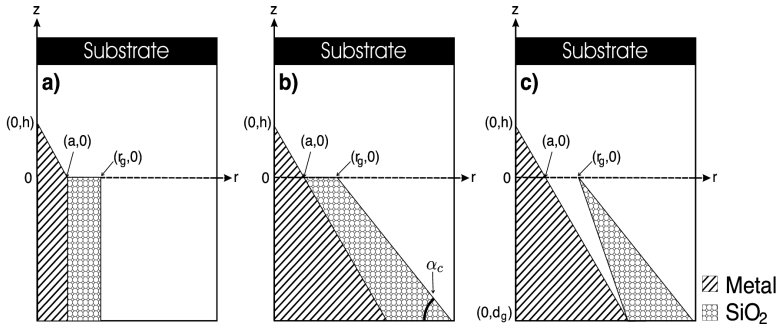
## Electrochemical Experiments and Combined AFM-SECM Measurements

All electrochemical experiments were performed with a commercial AFM, equipped with a quartz glass wet cell and a Ag/AgCl reference electrode. A commercial potentiostat or a homebuilt bipotentiostat (Based on a design proposed by Bard et al.<sup>8</sup>) were used to command the voltage and measure the currents for cyclic voltammetry and SECM measurements. In the mono-



**Figure 3.2:** Schematic representation of the setup. The conductive probe (working electrode) was mounted on a quartz glass cell and held in a meniscus of electrolyte between the glass cell and the sample. The reference electrode was emended into a channel of the glass cell, whereas the counter electrode was within the sample.

potentiostat configuration (figure 3.2) the sample was used as a combined counter electrode and substrate. The sample consisted of a  $1 \text{ cm}^2$  Si chip coated with a 200 nm thick  $\text{Si}_3\text{N}_4$  film onto which several  $2 \mu\text{m}$  wide, 100 nm thick and 100nm spaced (edge to edge) Pt lines had been deposited by means of the lift-off technique. In the bipotentiostat setup the sample was highly oriented pyrolytic graphite (HOPG) which served as second working electrode. A Pt wire was employed as counter electrode. In both setups the AFM-SECM probe was mounted to the quartz glass cell and held in a meniscus of electrolyte formed between the quartz glass cell and the sample surface. The reference electrode contacted the electrolyte via a channel in the glass cell filled with electrolyte. The output of the (bi-)potentiostat was recorded with the data acquisition card of the AFM controller electronics. The bending of the cantilever was detected by means of laser beam



**Figure 3.3:** a) Shows the diagram of a conical electrode represented in cylindrical coordinates. For practical reasons the geometry of the simulation space shows only the very apex of the tip where  $z$  is the axis of symmetry. b) Same diagram for a tip with conically shaped insulation. c) like b) but for a tip with conically shaped insulation and corresponding more precisely to the real fabricated tips, i.e. showing a gap at the apex of the tip between the metal and the insulation.

deflection,<sup>44,45</sup> and was used for controlling the force feedback in the constant force mode. During the acquisition of the electrochemical data the AFM feedback was switched off and the tip scanned the sample at constant height.

### Finite Element Simulation

The theoretical models were simulated with the finite element-modeling package FEMLAB. The geometry of conical tips with cylindrically shaped insulation (figure 3.3a) is described by the radius  $a$  at the base of their cone, the cone height  $h$  and the insulation radius  $r_g$ . For tips with conical insulation (figure 3.3b) we need to consider the cone angle  $\alpha_c$ . For an additional gap between insulation and metal (figure 3.3c) the gap depth  $d_g$  must be taken into account. The calculations were performed with values normalized to the base radius:  $H = h/a$ ,  $RG = r_g/a$ ,  $DG = d_g/a$ . The redox reaction, taking place at a finite conical electrode surface surrounded by insulation is modeled to be entirely dominated by diffusion.<sup>9,11</sup> For practical reasons the

steady state diffusion equation is solved in the cylindrical coordinate system:

$$D^* \left( \frac{\partial^2 c}{\partial r^2} + \frac{1}{r} \frac{\partial c}{\partial r} + \frac{\partial^2 c}{\partial z^2} \right) = 0, \quad (3.1)$$

where  $r$  and  $z$  are the coordinates in direction parallel and normal to the electrode base plane, respectively (see figure 3.3),  $D^*$  is the diffusion constant of the reactive species and  $c(r, z)$  its concentration. The diffusion-limited current was found by solving equation (3.1) with the following boundary conditions:

A) Exposed metal surface of the tip:

$$c = 0, \quad (3.2)$$

B) Insulated area of the Tip:

$$\frac{\partial c}{\partial \nu} = 0, \quad (3.3)$$

where  $\nu$  is the normal vector to the respective surfaces.

C) Simulation borders which are sufficiently far away from the tip in order to allow the bulk concentration to recover naturally:

$$c = c^*, \quad (3.4)$$

where  $c^*$  is the bulk concentration of the reactive species.

D) Depending on the reactivity of the substrate,

$$c = c^* \quad (3.5)$$

was selected for an electrically conductive substrate and

$$\frac{\partial c}{\partial z} = 0 \quad (3.6)$$

for an electrically insulating substrate. The electrochemical current generated at the electrode surface was obtained by integrating the flux over the area of the exposed metal cone.<sup>9</sup>

---

	H=1.5	H=2	H=2.5	H=3
A	1.4874	1.6769	1.8677	2.0585
B	0.4018	0.5240	0.7075	0.8910
C	0.3150	0.1794	-0.0053	-0.1900
D	-0.9647	-0.9857	-1.0073	-1.0288

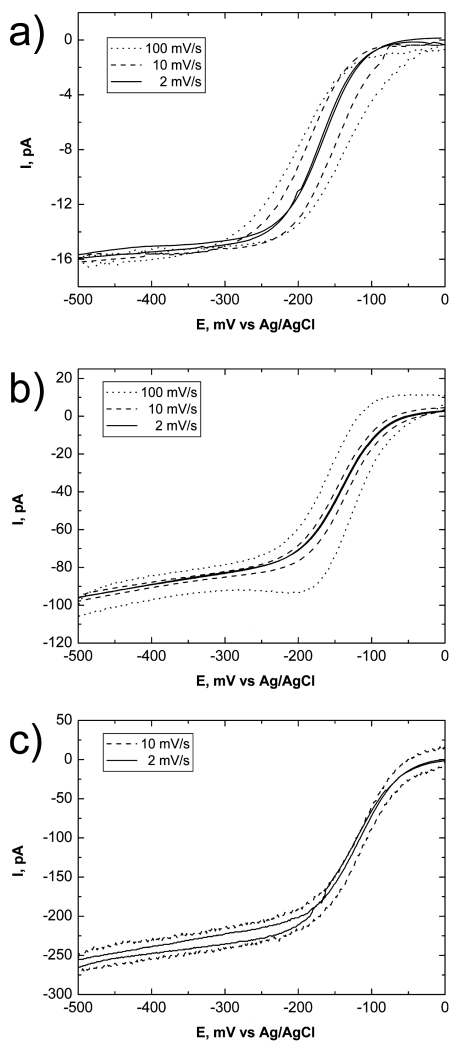
---

**Table 3.2:** Numerical constants as indicated by Zoski and Mirkin,<sup>10</sup> where the values for H=2.5 were interpolated.

### 3.1.3 Experimental and Simulation Results

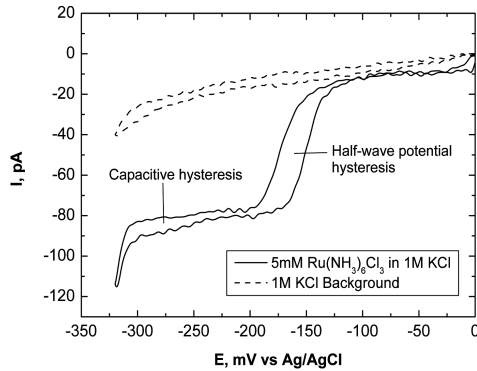
#### Cyclic Voltammetry

Figure 3.4 represents the cyclic voltammograms (CV) for 3 different tip sizes recorded in 5mM  $\text{Ru}(\text{NH}_3)_6\text{Cl}_3$  ( $332 \text{ nm}^3/\text{molecule}$ ) with 1M KCl in aqueous solution. The CV in figure 3.4a was acquired with the tip shown in figure 3.1e. In order track down the source of the capacitive and half-wave potential hysteresis between the back and the forward sweep, the CV's were performed at different rates (100mV/s, 10mV/s and 2mV/s). The results clearly show that the both hysteresis decreased when increasing the sweep rate. Figure 3.5 shows the CV of a  $\text{Pt}_x\text{Si}_y$  tip with gap (figure 3.1c) in the same electrolyte as described in the previous measurement, and in addition a background CV in 1M KCl aqueous solution only. The signal was recorded at a sweep rate of 2mV/s and showed a half-wave potential hysteresis between the forward and backward sweep direction. Due to the comparison with the TEM micrographs and following the indications of Zoski et al.<sup>9</sup> we attribute the half-wave potential hysteresis to the imperfect sealing between the  $\text{SiO}_2$  and the tip metal. The capacitive hysteresis was attributed to the thin insulation film encapsulating the metal lines of the cantilever.<sup>14</sup> Table 3.1 shows the estimated capacitances of the measured probes. All CVs showed a plateau in the voltage range of the redox reaction. The recorded



**Figure 3.4:** a) shows the cyclic voltammogram for the  $\text{Pt}_x\text{Si}_y$  tip (figure 3.1e) in 5mM  $\text{Ru}(\text{NH}_3)_6\text{Cl}_3$  with 1M KCl. b) and c) are the voltammogram for two similar  $\text{Pt}_x\text{Si}_y$  tips performed under the same conditions described in a). The voltammograms were recorded with different sweep rates.





**Figure 3.5:** Cyclic voltammogram for a  $Pt_xSi_y$  tip with gap (figure 3.1c) performed in 5mM  $Ru(NH_3)_6Cl_3$  ( $332 \text{ nm}^3/\text{molecule}$ ) and 1M KCl, 1M KCl background. This voltammograms were acquired at a sweep rate of 2mV/s.

steady state diffusion current  $I_{T,\infty}$  for the tip at an infinite distance from the surface held at the redox potential of  $Ru(NH_3)_6Cl_3$  ( $V_R = -230 \text{ mV}$ ) was deduced from the corresponding CV's (figures 3.4 and 3.5) and reported in table 3.1. The electric currents were between 14pA and 220pA. The theoretical steady-state diffusion current for a conical tip apex on a cylindrically shaped insulation (figure 3.3a) is given by<sup>10</sup>

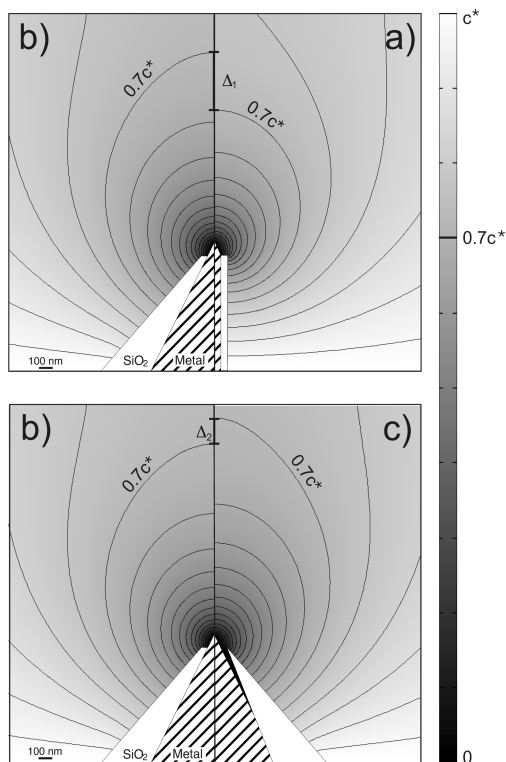
$$I_{T,\infty} = 4nFD^*c^*a(A + B(RG - C)^D) \quad (3.7)$$

where  $n$  is the number of electrons transferred during the reaction,  $F$  the Faraday constant,  $D^*$  the diffusion constant of  $Ru(NH_3)_6Cl_3$  ( $D^* = 5.3 * 10^{-6} \frac{\text{cm}^2}{\text{s}}$ ) (Ref.<sup>9</sup>),  $c^*$  the bulk concentration of  $Ru(NH_3)_6Cl_3$  ( $c^* = 5 \text{ mM}$ ). A,B,C and D are numerical constants as indicated by Zoski and Mirkin<sup>10</sup> (see table 3.2). The diffusion currents  $I_{T,\infty}$  and the related concentration gradients were obtained by solving the previously described finite element simulation model. The simulations were also carried out for the standard conical tip with a cylindrical insulation.<sup>10,11</sup> To investigate the influence of a

gap between tip and insulation, the simulation were solved for tips with and without a gap. The simulated steady state diffusion current for the cylindrically insulated tip (figure 3.3a) was 1.25 times higher than the current of the conically insulated tip (figure 3.3b). This can be caused by a better access from the side for the tube shaped probe and a therefore higher current. The simulated steady state diffusion current for the conically insulated tip with gap (figure 3.3c) also showed a 1.03 times higher current than the conically insulated tip without gap, which is due to the bigger exposed metal surface. For this reason the currents calculated with equation 3.7 had to be corrected by the corresponding proportionality factor (0.8 for conical insulation, figure 3.3b; 0.824 for conical insulation and gap, figure 3.3c). These corrected values were summarized in table 3.1 together with the respective tip base radii  $a_{CV}$  deduced from the measured redox current. The values of  $a_{CV}$  were within 50% of the geometrical values obtained from the TEM micrographs.

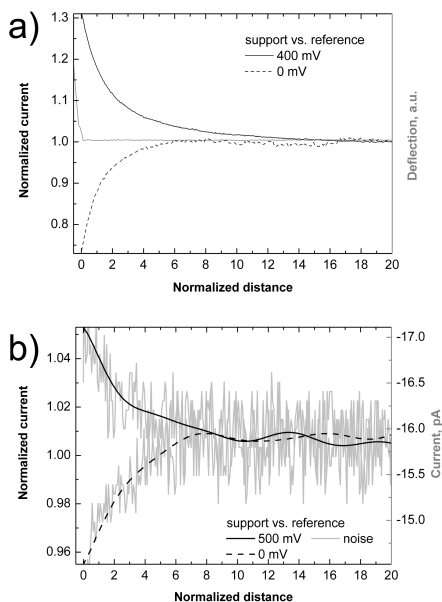
### SECM Simulations and Measurements

Figure 3.6 shows the simulated concentrations for the three models (figure 3.3), when the probe is at an infinite distance from the substrate. The lines are iso-concentration curves. For a conically insulated tip (figure 3.6b) the 70% line is further away ( $\Delta_1$ ) from the tip than for a cylindrically insulated tip (figure 3.6a) and hence, the probe with a conical insulation is supposed to sense the surface earlier when approaching to the sample. When we compare the conically insulated tip (figure 3.6b) with one that has the same insulation but with a gap (figure 3.6c), the shift is smaller ( $\Delta_2 < \Delta_1$ ) and in favor of the tip with gap. Consequently, the later should sense the surface even earlier. In SECM feedback experiments the electrochemical current is measured as function of the probe to sample distance. In our case, we could additionally record the cantilever deflection, i.e. the force interaction between the probe and the sample. The point of contact could be defined thereby. For each one of the presented approach curves the measured currents and distances were normalized; The normalized current is  $I = I_T / I_{T,\infty}^*$ , where  $I_{T,\infty}^*$  is the steady state redox current obtained from the respective voltammograms, recorded prior to the approach; the normalized distance is  $L = l/a$ , where the tip base radius  $a$  was deduced from the TEM micrographs and  $l$  is the tip



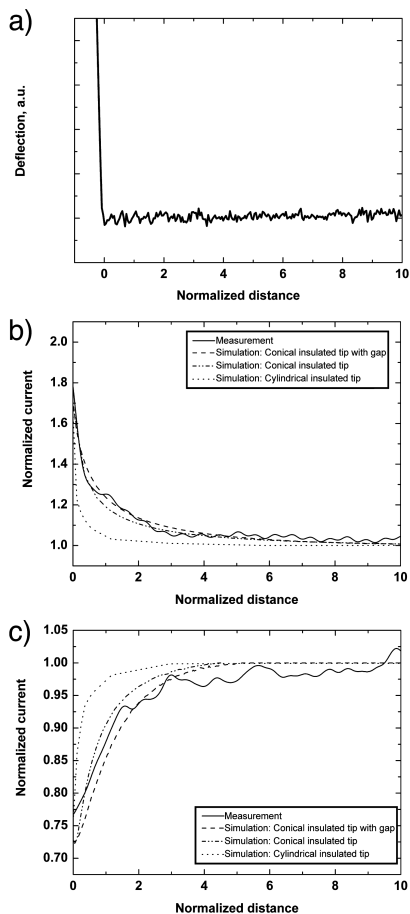
**Figure 3.6:** Simulated concentrations for the three models presented in figure 3.3, for a probe at an infinite distance from the substrate. The lines of equal concentration are spaced by  $0.05c^*$ . a) Tip with a cylindrical insulation; b) conical insulation; c) conical insulation with gap between the insulation and metal.

to sample distance. Figure 3.7 shows several AFM-SECM approach curves towards HOPG recorded in 5mM  $\text{Ru}(\text{NH}_3)_6\text{Cl}_3$  with 1M KCl using the bipotentiostat setup. The tip potential was set to  $-300\text{mV}$  vs. the  $\text{Ag}/\text{AgCl}$  reference electrode and the substrate was linearly approached towards the tip. The contact point was derived from the deflection signal. Positive and negative feedback on HOPG were achieved by adjusting the sample voltage.<sup>12</sup>

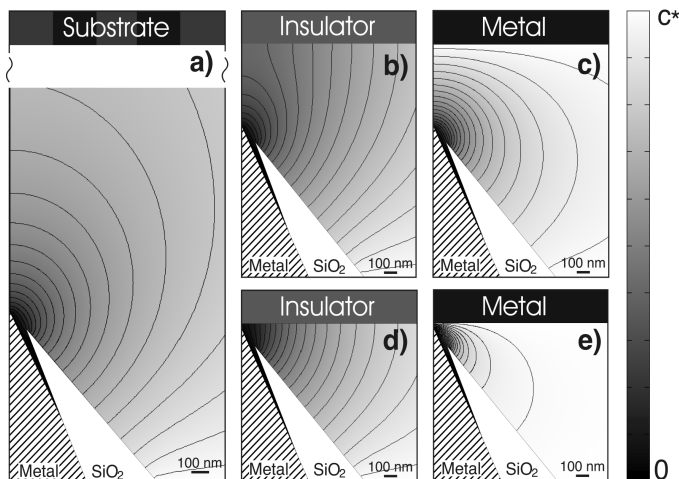


**Figure 3.7:** a) Combined AFM-SECM approach curves towards conductive graphite (HOPG) acquired in 5mM  $\text{Ru}(\text{NH}_3)_6\text{Cl}_3$  with 1M KCl. The tip potential was held at -300mV vs. an Ag/AgCl reference electrode and the HOPG was set to 0 mV for a negative feedback and at 400mV for a positive feedback. The deflection signal shows the contact point. b) like a) but for a smaller tip surface and a voltage of 500mV for the positive feedback. The lines are the raw data (0.75pA peak to peak) which was smoothed by 10Hz low pass filter. All curves contain 512 data points and were recorded with an approach time of 1s.

For sample voltages  $\leq 0$  mV a negative feedback was observed, whereas voltages  $\geq 300$ mV resulted in a positive feedback. The voltage needed to achieve positive feedback was higher for smaller electrode dimensions.<sup>8</sup> Figure 3.7a was recorded with a tip which gave a redox current of about 220pA (tip 3 on table 3.1). For tips with lower redox currents ( $< 100$ pA) in the CVs (tip 1 on table 3.1), the approach curves were noisier, however, still



**Figure 3.8:** Simultaneous AFM-SECM approach curves of the  $\text{Pt}_x\text{Si}_y$  probe onto Pt (b) and on  $\text{Si}_3\text{N}_4$  (c) in 5mM  $\text{Ru}(\text{NH}_3)_6\text{Cl}_3$  with 1M KCl. The tip potential was set to -240nm vs. an Ag/AgCl reference electrode. The simultaneously acquired deflection signal (a) shows the contact point. The dotted lines show the simulation results for a conical tip with a cylindrical insulation, conical insulation and conical insulation with a gap between the insulation and the metal. All curves show 512 data points and were recorded with an approach time of 1s.



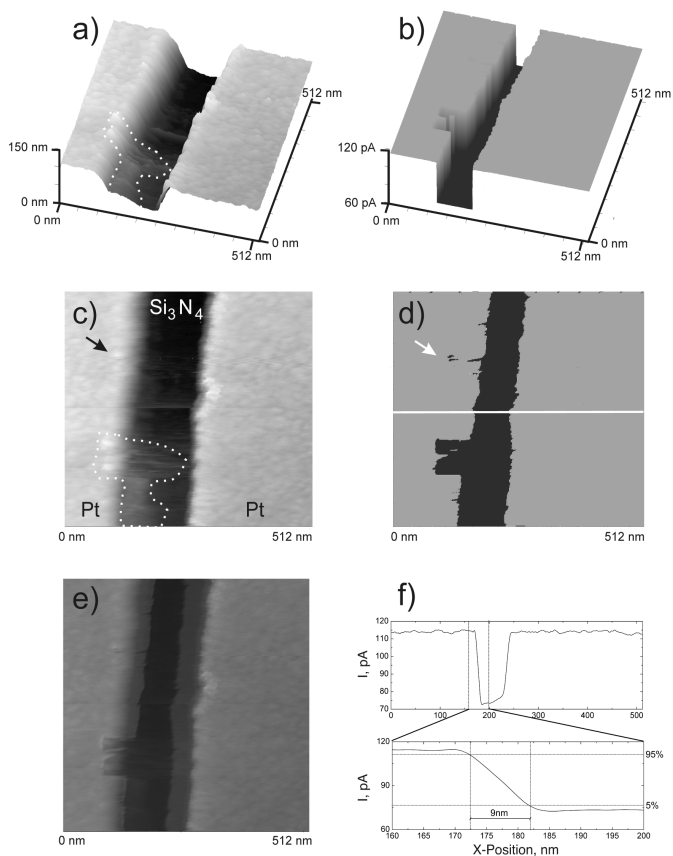
**Figure 3.9:** Simulation results for a conical tip similar to the fabricated probes, a) at an infinite distance from the substrate; b) and c) at 400nm from an insulating/conducting substrate; d) and e) at 50 nm from an insulating/conducting substrate.

showed a positive and negative feedback (figure 3.7b). The noise (0.75pA peak to peak) was due to a limitation of the amplifier. After the measurement, the data was therefore smoothed by a 10Hz low pass filter. Figure 3.8 shows approach curves in 5mM  $\text{Ru}(\text{NH}_3)_6\text{Cl}_3$  with 1M KCl, towards the conducting and insulating part of the combined sample and counter electrode (tip 4 on table 3.1). These measurements were performed with the monopotentiostat. The tip potential was set to  $-240\text{mV}$ . The substrate was linearly approached towards the tip and the contact point was again derived from the deflection signal (figure 3.8a). The current decreased/increased, when the tip came into proximity of the insulating/conducting surface. It was not necessary to apply an additional potential to the substrate. The approach curves were simulated with the finite element method described in the previous paragraph. The simulated concentration for several different distances from the conductive/insulating substrate for the conically insulated

tip with gap (figure 3.3c) is shown in figure 3.9. The concentration gradient increased/decreased when approaching a conductive/insulating substrate resulting in a positive/negative feedback. Figure 3.8 shows the simulated approach curves for the three models presented in figure 3.3. The geometrical parameters were chosen in order to show the same aspect ratios as the  $\text{Pt}_x\text{Si}_y$  tip for which the experimentally measured approach curve is plotted on the same graph. The simulated approach curves for the cylindrically insulated tip (figure 3.3a) has a later onset and shows a steeper increase/decrease of current compared to the approach curves for the conically insulated probes (figure 3.3b and c). The simulated approach curves of the probe with gap showed a further decrease in steepness. Therefore we conclude that the influence of the gap on the shape of the approach curve is less than the influence of the insulation cone angle. These results are in agreement with the simulated concentration profiles (figure 3.6), i.e. the conically insulated tip with gap senses the surface earlier. The experimentally acquired curves agreed well with the simulated curves for a conical insulation. However, the presence of a gap could not be derived from these measurements only.

### Combined AFM-SECM

Figure 3.10 shows sequentially recorded images (first topography, then electrochemical current) of Pt lines deposited on  $\text{Si}_3\text{N}_4$  and spaced by 100 nm (edge to edge). The electrolyte was an aqueous solution of 5mM  $\text{Ru}(\text{NH}_3)_6\text{Cl}_3$  with 1M KCl. The  $\text{Pt}_x\text{Si}_y$  tip potential was set to -240mV vs. an Ag/AgCl reference electrode. For the electrochemical current image (figure 3.10b and d), the probe was scanned at 30 nm +/- 5 nm above the metal at a line scan rate of 1 line/sece. As the tip was out of contact the scan height was obtained from the calibrated piezo signal. The different distances are due to an imperfect parallelism of the sample surface to the scan plane. The dotted line and the arrow in figure 3.10a, c and d indicate contaminations spots, which hindered the positive feedback reaction on the Pt. These imperfections were used to correlate the topography and electrochemical current image. Figure 3.10e shows a superposition of the topography and electrochemical data. This representation shows that the space between the lines



**Figure 3.10:** Sequentially recorded AFM-SECM image (first topography, then electrochemical image) of Pt lines on insulator. For a better representation of the topography, the images are also shown in 3D: (a) and (c) topography; (b) and (d) electrochemical current image in 5mM  $\text{Ru}(\text{NH}_3)_6\text{Cl}_3$  with 1M KCl. The tip potential was set to -240mV vs. Ag/AgCl. The dotted lines in (a) and (c) emphasize dirt over the edge of the left Pt line, whereas the upper arrow points to a smaller dirt particle on the left Pt line. e) Superposition of topography (c) and electrochemical current image (d). f) Profile of the electrochemical current image along the horizontal line shown in (d). The distance between 5% and 95% of the electrochemical current step is 9nm and indicates a lateral electrochemical resolution below 10 nm. All images were recorded with 512x512 data points and the curve with 512 data points.



in the electrochemical image is smaller than in the topography. We attribute this to a positive feedback occurring between the sidewall of the lines and the tip when its position is between two metal lines. Figure 3.10f shows the profile of the electrochemical current image along the line in figure 3.10d. The distance between 5% and 95% of the electrochemical current step is 9nm. This indicates that a lateral electrochemical image resolution below 10 nm can be obtained.

### 3.1.4 Conclusion

The functionality of the presented AFM-SECM probes have been demonstrated by means of steady state cyclic voltammetry experiments, electrochemical approach curves and simultaneously recorded probe deflection curves. Sequentially acquired topographical and electrochemical images could be acquired. The experimental results demonstrated that even for probes with dimensions in the lower nanoscale domain, the simulation model introduced by Zoski et al. is still valid. However, the simulated diffusion current  $I_{T,\infty}$  was overestimated by 25% for tips with conical insulation. The gap between the tip metal and insulation showed a small effect on the shape of the feedback curves compared to the influence of the cone angle of the insulation. Conically insulated tips showed an earlier onset and a flatter feedback in the approach curve when compared to cylindrically insulated tips. The size of the probe was narrow enough to acquire electrochemical current images with a lateral resolution below 10nm. This is comparable to the topographical resolution achieved with the same probe. Such AFM-SECM probes could be helpful for studying e.g. samples in electrochemistry, cell and structural biology, where the electrochemical active spots are in the nanometer scale range. For such applications, both, localizing the site and analyzing its topography is important for studying it's biological function.

## Bibliography

1. Bard, A. J.; Fan, F. R. F.; Kwak, J.; Lev, O. ; Scanning Electrochemical Microscopy. Introduction and Principles., *Anal. Chem.* **1989**, *61*, 132-138.
2. Bard, A. J.; Fan, F. R. F.; Pierce, D. T.; Unwin, P. R.; Wipf, D. O.; Zhou, F. M. ; Chemical Imaging of Surfaces with the Scanning Electrochemical Microscope, *Science* **1991**, *254*, 68-74.
3. Mirkin, M. V.; Fan, F. R. F.; Bard, A. J. ; Scanning Electrochemical Microscopy. 13. Evaluation of the Tip Shape of Nanometer Size Microelectrodes, *J. Electroanal. Chem.* **1992**, *328*, 47-62.
4. Bard, A. J.; Fan, F. R. F.; Mirkin, M. V. *Electroanalytical Chemistry a Series of Advances Vol. 18*; volume 18 Marcel Dekker: New York, 1994.
5. Mirkin, M. V. ; High resolution studies of heterogeneous processes with the scanning electrochemical microscope, *Mikrochim. Acta* **1999**, *130*, 127-153.
6. Macpherson, J. V.; Unwin, P. R. ; Combined scanning electrochemical-atomic force microscopy, *Anal. Chem.* **2000**, *72*, 276-285.
7. Bard, A. J.; Mirkin, M. V. *Scanning Electrochemical Microscopy*; Marcel Dekker: New York, NY, 2001.
8. Bard, A. J.; Faulkner, L. R. *Electrochemical Methods, Fundamentals and Applications*; Wiley and Sons: New York, NY, 2001.
9. Zoski, C. G. ; Ultramicroelectrodes: Design, fabrication, and characterization, *Electroanalysis* **2002**, *14*, 1041-1051.
10. Zoski, C. G.; Mirkin, M. V. ; Steady-state limiting currents at finite conical microelectrodes, *Anal. Chem.* **2002**, *74*, 1986-1992.
11. Zoski, C. G.; Liu, B.; Bard, A. J. ; Scanning electrochemical microscopy: Theory and characterization of electrodes of finite conical geometry, *Anal. Chem.* **2004**, *76*, 3646-3654.

12. Wipf, D. O.; Bard, A. J.; Scanning Electrochemical Microscopy. 7. Effect of Heterogeneous Electron-Transfer Rate at the Substrate on the Tip Feedback Current, *J. Electrochem. Soc.* **1991**, *138*, 469-474.
13. Ervin, E. N.; White, H. S.; Baker, L. A.; Alternating current impedance imaging of membrane pores using scanning electrochemical microscopy, *Anal. Chem.* **2005**, *77*, 5564-5569.
14. Frederix, P. L. T. M.; Gullo, M. R.; Akiyama, T.; Tonin, A.; de Rooij, N. F.; Staufer, U.; Engel, A.; Assessment of insulated conductive cantilevers for biology and electrochemistry, *Nanotechnology* **2005**, *16*, 997-1005.
15. Abe, T.; Itaya, K.; Uchida, I.; An Electrochemical Fabrication Method for Gold and Carbon Ultramicroelectrode, *Chem. Lett.* **1988**, 399-402.
16. Gewirth, A. A.; Craston, D. H.; Bard, A. J.; Fabrication and Characterization of Microtips for Insitu Scanning Tunneling Microscopy, *J. Electroanal. Chem.* **1989**, *261*, 477-482.
17. Nagahara, L. A.; Thundat, T.; Lindsay, S. M.; Preparation and Characterization of STM Tips for Electrochemical Studies, *Rev. Sci. Instrum.* **1989**, *60*, 3128-3130.
18. Potje-Kamloth, K.; Janata, J.; Josowicz, M.; Electrochemically prepared insulation for carbon fiber microelectrodes, *Ber. Bunsenges. Phys. Chem.* **1989**, *93*, 1480-1491.
19. Penner, R. M.; Heben, M. J.; Longin, T. L.; Lewis, N. S.; Fabrication and use of Nanometer-Sized Electrodes in Electrochemistry, *Science* **1990**, *250*, 1118-1121.
20. Vitus, C. M.; Chang, S. C.; Schardt, B. C.; Weaver, M. J.; Insitu Scanning Tunneling Microscopy as a Probe of Adsorbate-induced Reconstruction at Ordered Monocrystalline Electrodes - Co on Pt (100), *J. Phys. Chem.* **1991**, *95*, 7559-7563.

21. Strein, T. G.; Ewing, A. G. ; Characterization of Submicron-Sized Carbon Electrodes Insulated with a Phenol Allylphenol Copolymer, *Anal. Chem.* **1992**, *64*, 1368-1373.
22. Bach, C. E.; Nichols, R. J.; Beckmann, W.; Meyer, H.; Schulte, A.; Besenhard, J. O.; Jannakoudakis, P. D. ; Effective Insulation of Scanning-Tunneling-Microscopy Tips for Electrochemical Studies Using an Electropainting Method, *J. Electrochem. Soc.* **1993**, *140*, 1281-1284.
23. Zhang, B. L.; Wang, E. K. ; Fabrication of STM Tips with Controlled Geometry by Electrochemical Etching and ECSTM Tips Coated with Paraffin, *Electrochim. Acta* **1994**, *39*, 103-106.
24. Schulte, A.; Chow, R. H. ; Cylindrically etched carbon-fiber microelectrodes for low-noise amperometric recording of cellular secretion, *Anal. Chem.* **1998**, *70*, 985-990.
25. Slevin, C. J.; Gray, N. J.; Macpherson, J. V.; Webb, M. A.; Unwin, P. R. ; Fabrication and characterisation of nanometre-sized platinum electrodes for voltammetric analysis and imaging, *Electrochem. Commun.* **1999**, *1*, 282-288.
26. Conyers, J. L.; White, H. S. ; Electrochemical characterization of electrodes with submicrometer dimensions, *Anal. Chem.* **2000**, *72*, 4441-4446.
27. Binnig, G.; Quate, C. F.; Gerber, C. ; Atomic Force Microscope, *Phys. Rev. Letts.* **1986**, *56*, 930-933.
28. Bonnell, D. *Scanning Probe Microscopy and Spectroscopy, Theory, Techniques and Applications*; Wiley-VHX: New York, NY, 2000.
29. Macpherson, J. V.; Unwin, P. ; Noncontact electrochemical imaging with combined scanning electrochemical atomic force microscopy, *Anal. Chem.* **2001**, *73*, 550-557.
30. Dobson, P. S.; Weaver, J. M. R.; Holder, M. N.; Unwin, P. R.; Macpherson, J. V. ; Characterization of batch-microfabricated scanning

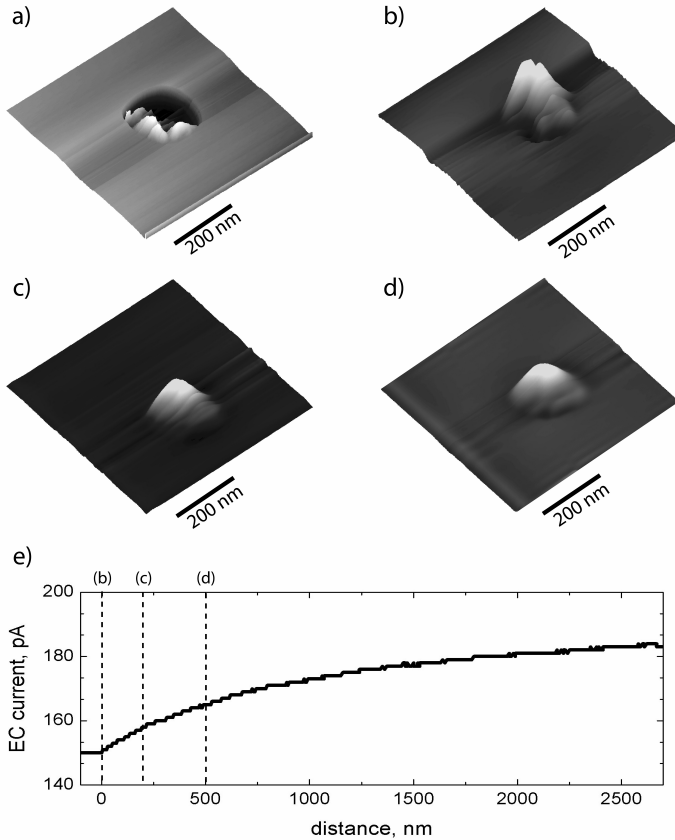
- electrochemical-atomic force microscopy probes, *Anal. Chem.* **2005**, *77*, 424-434.
31. Ludwig, M.; Kranz, C.; Schuhmann, W.; Gaub, H. E. ; Topography Feedback Mechanism for the Scanning Electrochemical Microscope Based on Hydrodynamic-Forces Between Tip and Sample, *Rev. Sci. Instrum.* **1995**, *66*, 2857-2860.
  32. James, P. I.; Garfias-Mesias, L. F.; Moyer, P. J.; Smyrl, W. H. ; Scanning electrochemical microscopy with simultaneous independent topography, *J. Electrochem. Soc.* **1998**, *145*, L64-L66.
  33. Buchler, M.; Kelley, S. C.; Smyrl, W. H. ; Scanning electrochemical microscopy with shear force feedback - Investigation of the lateral resolution of different experimental configurations, *Electrochem. Solid State Lett.* **2000**, *3*, 35-38.
  34. Kranz, C.; Friedbacher, G.; Mizaikoff, B. ; Integrating an ultramicro-electrode in an AFM cantilever: Combined technology for enhanced information, *Anal. Chem.* **2001**, *73*, 2491-2500.
  35. Kranz, C.; Kueng, A.; Lugstein, A.; Bertagnolli, E.; Mizaikoff, B. ; Mapping of enzyme activity by detection of enzymatic products during AFM imaging with integrated SECM-AFM probes, *Ultramicroscopy* **2004**, *100*, 127-134.
  36. Kueng, A.; Kranz, C.; Mizaikoff, B.; Lugstein, A.; Bertagnolli, E. ; Combined scanning electrochemical atomic force microscopy for tapping mode imaging, *Appl. Phys. Lett.* **2003**, *82*, 1592-1594.
  37. Holder, M. N.; Gardner, C. E.; Macpherson, J. V.; Unwin, P. ; Combined scanning electrochemical-atomic force microscopy (SECM-AFM): Simulation and experiment for flux-generation at un-insulated metal-coated probes, *J. Electroanal. Chem.* **2005**, *585*, 8-18.
  38. Gardner, C. E.; Unwin, P. R.; Macpherson, J. V. ; Correlation of membrane structure and transport activity using combined scan-

- ning electrochemical-atomic force microscopy, *Electrochem. Commun.* **2005**, *7*, 612-618.
39. Holt, K. B.; Bard, A. J.; Show, Y.; Swain, G. M. ; Scanning electrochemical microscopy and conductive probe atomic force microscopy studies of hydrogen-terminated boron-doped diamond electrodes with different doping levels, *J. Phys. Chem. B* **2004**, *108*, 15117-15127.
  40. Gullo, M. R.; Akiyama, T.; de Rooij, N. F.; Staufer, U.; Tonin, A.; Engel, A.; Frederix, P. L. T. M. ; Insulated conductive cantilevers for in situ experiments in structural biology, *12th Int. Conf. on Scanning Tunneling Microscopy/Spectroscopy and Related Techniques* **2003**, 166-171.
  41. Akiyama, T.; Gullo, M. R.; de Rooij, N. F.; Tonin, A.; Hidber, H. R.; Frederix, P. L. T. M.; Engel, A.; Staufer, U. ; Development of insulated conductive probes with platinum silicide tips for atomic force microscopy in cell biology, *Japan. J. Appl. Phys. Part 1-Regular Papers Short Notes & Review Papers* **2004**, *43*, 3865-3867.
  42. Akamine, S.; Quate, C. F. ; Low-Temperature Thermal-Oxidation Sharpening of Microcast Tips, *J. Vac. Sci. & Technol. B* **1992**, *10*, 2307-2310.
  43. Albrecht, T. R.; Akamine, S.; Carver, T. E.; Quate, C. F. ; Microfabrication of Cantilever Styli for the Atomic Force Microscope, *J. Vac. Sci. & Technol. A-Vacuum Surfaces and Films* **1990**, *8*, 3386-3396.
  44. Meyer, G.; Amer, N. M. ; Novel Optical Approach to Atomic Force Microscopy, *Appl. Phys. Lett.* **1988**, *53*, 1045-1047.
  45. Meyer, G.; Amer, N. M. ; Optical-Beam-Deflection Atomic Force Microscopy - The NaCl (001) Surface, *Appl. Phys. Lett.* **1990**, *56*, 2100-2101.

## 3.2 Latest Results

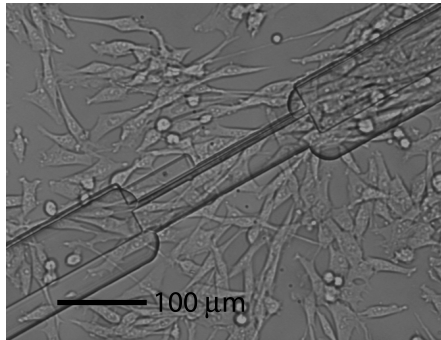
### 3.2.1 First Combined AFM-SECM Experiments on the Planar Sample Support and Biological Cells

First combined AFM-SECM measurements on the planar sample support were performed with the same setup described in the previous section. Again the redox mediator was an aqueous solution of 5mM  $\text{Ru}(\text{NH}_3)_6\text{Cl}_3$  and 1M KCl. The AFM was operated in the so-called linear lift mode where for each line first a scan in contact and then a scan at a defined constant and tilt corrected height above the sample surface was performed. In this experiment the counter electrode was not incorporated in the sample and therefore the contrast of the electrochemical images was provided only by a negative feedback (figure 3.11e). Figures 3.11a and 3.11b show the simultaneously acquired topography and electrochemical current image of the microfabricated aperture in the planar sample support, respectively. When the tip was in contact with the surface the diffusion of redox mediator towards the scanning tip was blocked, however when the tip was above the aperture the blocking was reduced, which resulted in a higher current. Furthermore, the dirt particles on the left of the aperture rim additionally blocked the diffusion towards the sidewalls of the exposed metal tip and resulted in a drop of current in the electrochemical current image (figure 3.11b). Figures 3.11c and 3.11d show the electrochemical current as the tip was scanned at 200nm and 500nm above the surface, respectively. The images still show an electrochemical current, however, with less contrast and details. The next step was to make combined AFM-SECM measurements on biological cells absorbed onto the planar sample support. But first it was necessary to examine the biocompatibility of the sample support. Figure 3.12 shows a microscope picture of baby hamster kidney cells grown on the sample support during 1 day in an incubator. The biological cells liked the substrate and grew without any difficulty. In order to preserve the cell structure for further experiments they were fixed for 15min with 4% formalin in phosphate buffered saline solution (PBS) and conserved in only PBS. Figure 3.13a and 3.13b show AFM micrographs of fixed fibroblasts (Rat2 and Cos7 respecti-



**Figure 3.11:** AFM-SECM images on the planar sample support: a) Contact AFM image of the aperture on the planar sample support (data scale range is  $5\mu\text{m}$ ); b) Electrochemical feedback image simultaneously measured with a), (data scale range is 150pA to 181pA); c) Electrochemical feedback image measured in linear lift mode at 200nm above the surface (data scale range is 159pA to 183pA); d) Electrochemical feedback image measured in linear lift mode at 500nm above the surface (data scale range is 166pA to 185pA); e) Approach curve showing the negative feedback, the dotted lines show the distances at which the images were taken.



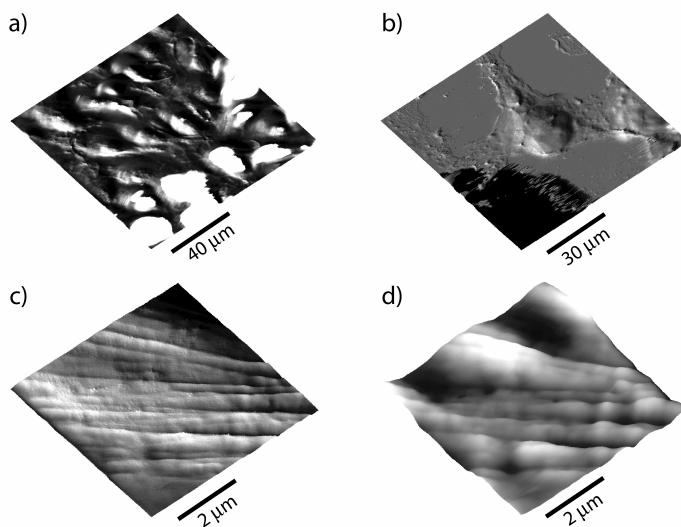


**Figure 3.12:** Microscope image of baby hamster kidney cells grown on the sample support. Courtesy of L. Sumanovsky, Biozentrum Basel.

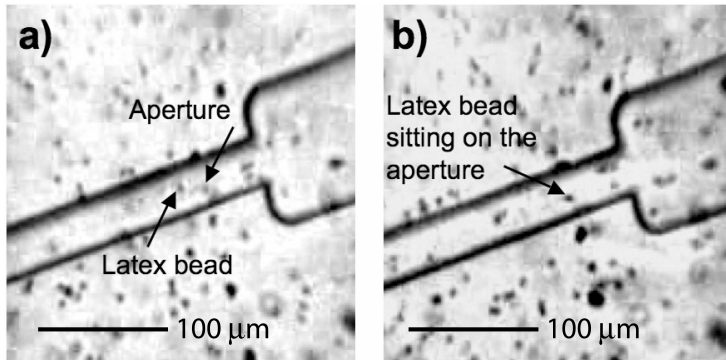
vely) grown on the planar sample support for 2 days and 1 day respectively. Figure 3.13c and 3.13d show simultaneously taken AFM-SECM measurements on fixed Cos7 fibroblasts immersed in 5mM  $\text{Ru}(\text{NH}_3)_6\text{Cl}_3$  with 1M KCl in aqueous solution. The setup used for this experiment is the same described earlier in this section. Again the AFM was operated in linear lift mode and the electrochemical image in figure 3.13d was recorded at 200nm above the surface. After 30min of measurement the fixed cells began to fall apart everywhere on the support.

### 3.2.2 Venturi Effect with the Planar Sample Support

An important step was to investigate how to attach biological cells onto the aperture in the planar sample support. One method is to aspirate the cells by means of the Venturi effect: The drawing of a liquid through the micro machined channel beneath the aperture generates a lower pressure in the channel and thus generates a flow gradient towards the hole. To induce the Venturi effect the planar sample support was connected to a peristaltic pump. The channel was filled with filtered (100nm filter) DI water and latex micro beads ( $1\mu\text{m}$  in diameter) were suspended in a drop of the same DI water. The peristaltic pump was operated in order to draw  $0.3\mu\text{l}/\text{min}$  through the channel. Figure 3.14a and 3.14b are snapshots of a movie recorded dur-



**Figure 3.13:** AFM and combined AFM-SECM measurements on biological cells: a) Fixed Rat2 fibroblasts (data scale range  $5\mu m$ ); b) Fixed Cos7 fibroblast (data scale range  $5\mu m$ ); c) Fixed Cos7 fibroblast (data scale range  $1\mu m$ ) and simultaneously recorded electrochemical image (d) 200nm above the surface (data scale range 160pA to 186pA).



**Figure 3.14:** Venturi effect: a) Suspended  $1\mu\text{m}$  latex beads move along the flow gradient induced by the Venturi effect towards the aperture until a bead reaches the aperture (b).

ing the Venturi experiment. The beads were all pulled along the flow gradient towards the aperture. When the bead pointed out by the arrow in figure 3.14a reached the aperture the flow gradient dropped and the movement of the other beads stopped (figure 3.14b). By applying an overpressure to the channel system it was possible to remove the bead from the aperture and repeat the experiment.



## Chapter 4

# Summary, Conclusion and Outlook

### 4.1 Planar Sample Support Fabrication

The surface property of substrates for biological samples plays an important role. Indeed, the surface needs to be biocompatible or at least non toxic. From the AFM point of view the support must provide a good adhesion for cells in order to hold them still during scanning. The most important, however, is a low surface roughness of the support. Especially for imaging of 2D protein crystals the roughness must be as low as possible or at least lower than the height of the crystal layer. This has two reasons: First it helps localizing the membrane patches on the surface and second it is needed for achieving high resolution. This requirements had to be considered for the fabrication of the planar sample support. By molding the surface of a plain Si wafer it was possible to achieve a surface which was smooth enough for the desired application. In this case molding by CVD proofed to be a powerful technique to reproduce not only micrometer scaled structures but also nano and sub nanometer sized features.

In order to use the molded surface of the  $Si_3N_4$  we need to bond the micro channel system to the  $Si_3N_4$  surface layer and dissolve the sacrificial Si wafer in KOH. This last step required that the bonding resists KOH etching.

Special epoxy glues were investigated for bonding, but none of the epoxies resisted longer than 5h in KOH. Finally, anodic bonding was the solution. However, in order to decrease the capacitance of the support it was necessary to increase the thickness of the  $Si_3N_4$  what made anodic bonding difficult. Nevertheless, anodic bonding at temperatures near to the melting point of the used pyrex glass proofed to be suitable for bonding thick dielectric layers.

In the first generation of planar sample supports a final, controlled LPCVD deposition of  $Si_3N_4$  succeeded to shrink the aperture diameter. However, in our case this technique showed to have limitations: First, the deposition rates of standard machines could not be reduced in a way to control the deposition at the nanometer scale, a dedicated setup would therefore be needed; Second, the edges of the apertures became rounded. The aperture diameter was indeed in the nanometer scale, but had a funnel profile, which wasn't favorable for high resolution AFM; Third, the additional LPCVD deposition increased the surface roughness again. These were the major reasons that made it necessary to fabricate the apertures by e-beam lithography.

## 4.2 Experiments

The electrochemical characterization of the metal tips with cyclic voltammetry (CV), gave evidence that the portion of the metal in contact with the electrolyte was larger then predicted based on SEM pictures. It was therefore necessary to take transmission electron micrographs, which showed the presence of a gap between the metal tip and the surrounding insulation. CV proved to be a powerfull tool to test electrical insulations and estimate very precisely the amount of exposed conductive surface. The insulation of other parts of the setup have also been tested and several points of leakage could be found. This helped to drastically increase the quality and repeatability of the electrochemical experiments.

First combined AFM-SECM measurements at different distances above the aperture in the planar sample support clearly demonstrated the distance dependence of the contrast in the SECM imaging. It also proofed that the

used linear lift mode is probably the most suitable mode of combined AFM-SECM imaging.

First combined AFM-SECM on fibroblast cells adsorbed on the planar sample support showed a favorable adhesion of the cells and a correlation between topography and electrochemical image. However, further effort is needed to find the right electrolyte mixture in order to achieve a higher topographical resolution. Although the fibroblast were fixed, they didn't withstand the redox reaction and fall into pieces after some minutes. Also here more work is needed for finding a more suitable redox mediator.

Of course it is evident that a smaller tip electrode enables a higher electrochemical resolution. However, the amount of electrochemical current and the feedback contrast of the electrochemical image also decreases with the size of the tip. Also the noise in the measurements becomes a bigger issue. Most of the tips used for SECM experiments were already so small that the used amplifiers were working on their lower limits and the signal was nearly hidden in the noise. Therefore it will be necessary to develop a dedicated low noise bipotentiostat.

The finite element model used to simulate the concentration gradients and estimate the electrochemical currents proved to be accurate for diffusion limited system and fast reaction kinetics. Moreover, the correlation between measurements and numerical simulations showed that the model introduced by Zoski et al. is still valid for nanometric tips. It was also possible to confirm the effect of the tip shape on the SECM approach curves for positive and negative feedback. These kind of finite element simulations in electrochemistry might be a powerful tool to predict the shape of approach curves for any kind of electrode shape.

### **4.3 Outlook**

As a great endeavor has been undertaken to produce valuable probes and supports, obviously the next steps will focus on applications. Indeed, the presented setup offers the possibility of many experiments in the field of electrochemistry and biology. Future efforts will particularly focus on simultaneous imaging of topography and reactivity of redox active biological sam-

ples or diffusion through biological pores. Other applications like studying the chemical reactions on non biological surfaces could be achieved, i.e. characterization of nano electrodes or ion selective field effect transistors. Furthermore nanolithography by induced local oxidation or local polymerization of electro active resists can be envisaged.










**Part III**






**Appendix**

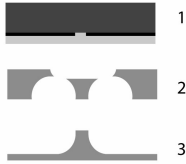


















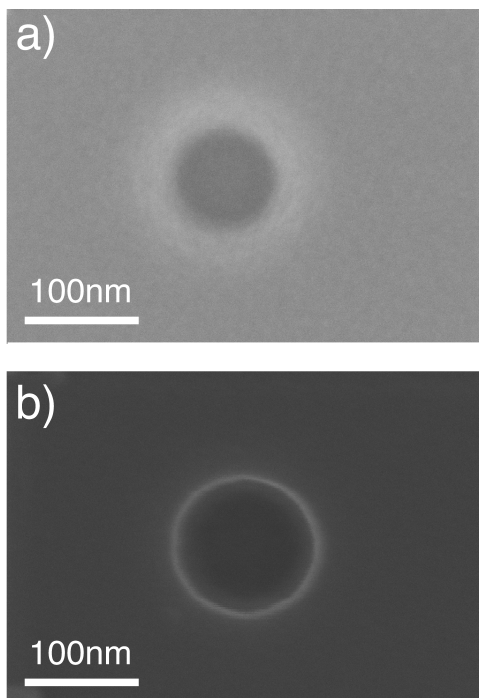
## **Appendix A**

# **Planar Sample Support Process Flow**

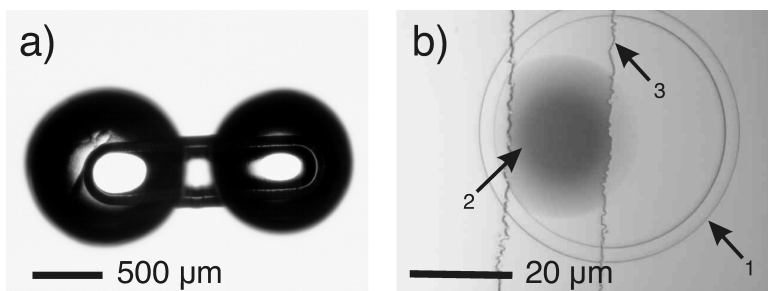
Fabrication of Pyrex Channels	
	2 x 200nm poly silicon on pyrex.
	Backside photolithography and RIE.
	Etching of the access holes in 50% HF.
	Topside photolithography and RIE.
	Etching of the top channel and access holes in 50% HF until contact.
	40% KOH to remove poly silicon mask
	

Fabrication of Top Chip	
	200nm Si <sub>x</sub> N <sub>y</sub> LPCVD low stress on Si wafer.
	E-beam lithography and RIE.
	600nm SiO <sub>2</sub> CVD on topside.
	Remove Si <sub>x</sub> N <sub>y</sub> on backside by RIE
 <span style="display: inline-block; width: 15px; height: 15px; background-color: black; margin-right: 5px;"></span> silicon-nitride <span style="display: inline-block; width: 15px; height: 15px; background-color: lightgray; margin-right: 5px; margin-left: 20px;"></span> silicon-dioxide <span style="display: inline-block; width: 15px; height: 15px; background-color: darkgray; margin-left: 20px;"></span> silicon	

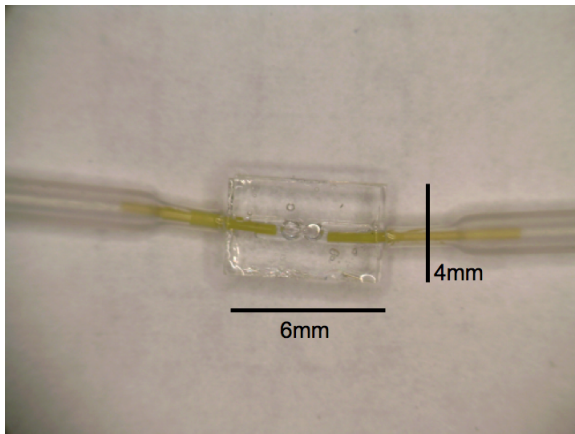
Assembling of the Chips			
 <p>1 2 3</p>	<p>1) Silicon-nitride (<math>\text{Si}_3\text{N}_4</math>) thin film deposited on a Si wafer with a nanoscaled aperture protected by silicon-dioxide (<math>\text{SiO}_2</math>). 2- 3) Pyrex chips with the fluidic network.</p>		
	<p>Part 1 and 2 are assembled by anodic bonding. The bonded chip is then glued to part 3 by means of an UV curable glue.</p>		
	<p>Release of the <math>\text{Si}_3\text{N}_4</math> membrane by dissolving the Si support in KOH (40%, 60°C)</p>		
	<p>The aperture is released by a timed etching of the <math>\text{SiO}_2</math> in buffered HF (BHF)</p>		
	<p>The channels in the pyrex chip are then accessed by fitting capillaries into the in- and outlet and fixing them with UV curable glue.</p>		
<table style="width: 100%; border: none;"> <tr> <td style="width: 50%; border: none;"> <p> silicon-nitride</p> <p> silicon</p> </td> <td style="width: 50%; border: none;"> <p> pyrex glass</p> <p> silicon-dioxide</p> </td> </tr> </table>		<p> silicon-nitride</p> <p> silicon</p>	<p> pyrex glass</p> <p> silicon-dioxide</p>
<p> silicon-nitride</p> <p> silicon</p>	<p> pyrex glass</p> <p> silicon-dioxide</p>		



**Figure A.1:** SEM micrographs: a) 100 nm aperture patterned in PMMA, b) the same aperture transferred into Si<sub>3</sub>N<sub>4</sub>



**Figure A.2:** Pictures of the fabricated chips: a) Top view of the pyrex channel chip; b) Si<sub>3</sub>N<sub>4</sub> film on Si, the ring and circle (1,2) are alignment structures for the AFM, the channel (3) is etched into the SiO<sub>2</sub>.

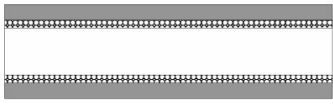
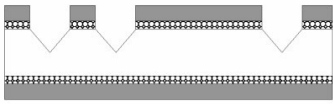
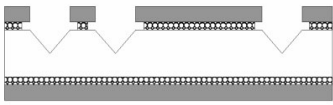
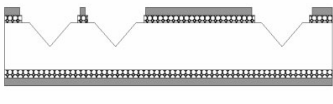
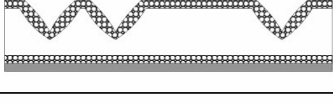
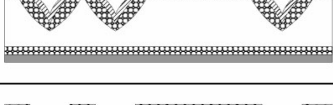
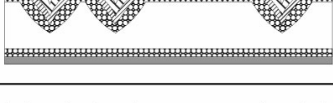

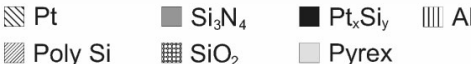


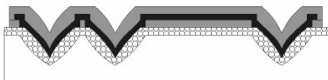
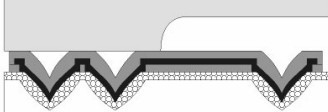
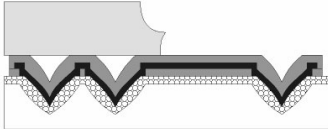
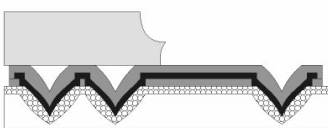
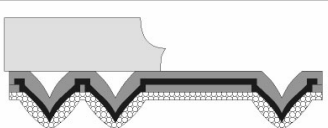
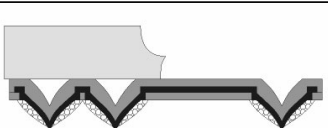
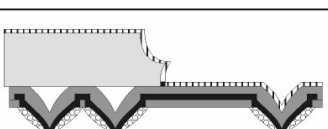





















**Figure A.3:** Picture of the assembled planar sample support

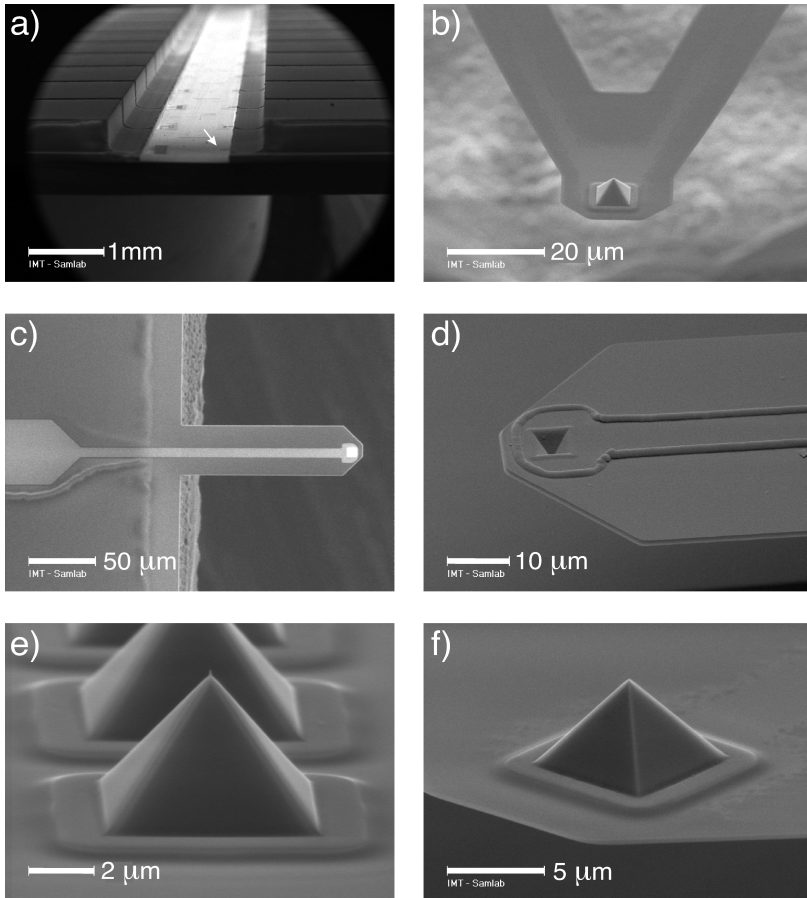


## **Appendix B**

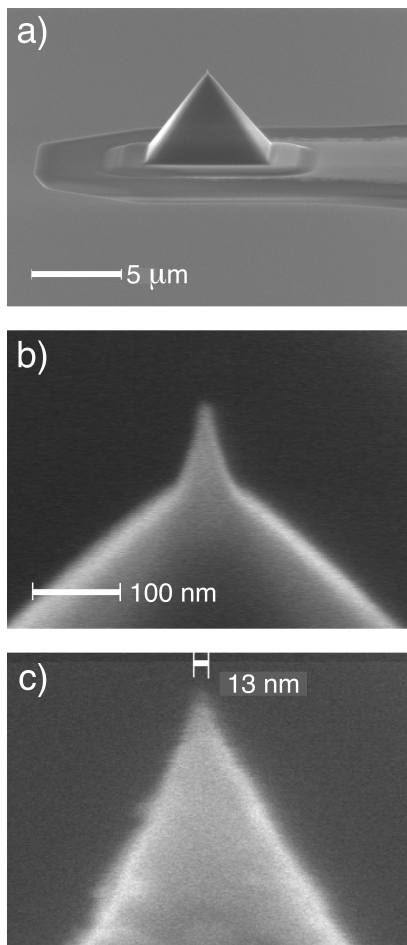
# **Conductive Probe Process Flow**

	Thermal oxidation (200nm, 1100°C) of a <111> Si wafer followed by 150nm low stress Si <sub>x</sub> N <sub>y</sub> LPCVD.
	Photolithography, RIE through the Si <sub>x</sub> N <sub>y</sub> and SiO <sub>2</sub> layer. KOH (40%, 60°C) to form the pyramidal tip mold.
	Timed BHF etch of the SiO <sub>2</sub> .
	Timed H <sub>3</sub> PO <sub>4</sub> etch of the Si <sub>x</sub> N <sub>y</sub> .
	Thermal oxide sharpening (1µm, 950°C).
	200nm poly-Si PECVD, photolithography patterning and RIE.
	500nm Pt evaporation and annealing (950°C) to form Pt <sub>x</sub> Si <sub>y</sub> .
	Ultrasound in isopropanol to remove unreacted Pt. 500nm low stress Si <sub>x</sub> N <sub>y</sub> LPCVD, photolithography and RIE patterning of the cantilever shape.
	

	<p>Blank RIE to remove <math>\text{Si}_x\text{N}_y</math> and <math>\text{SiO}_2</math> on the backside.</p>								
	<p>Anodic bonding (500°C, 600V, 200N) of a prediced pyrex glass wafer.</p>								
	<p>Backside KOH (40%, 60°C) etch of 3/4 of the Si wafer tikness.</p>								
	<p>Dicing for the release of the cantilever topside.</p>								
	<p>Release of the cantilever in KOH (40%, 60°C)</p>								
	<p>Opening of the tip apex by a timed etch in BHF.</p>								
	<p>Evaporation of a Al reflection layer.</p>								
<table border="0"> <tbody> <tr> <td> Pt</td> <td> <math>\text{Si}_3\text{N}_4</math></td> <td> <math>\text{Pt}_x\text{Si}_y</math></td> <td> Al</td> </tr> <tr> <td> Poly Si</td> <td> <math>\text{SiO}_2</math></td> <td> Pyrex</td> <td></td> </tr> </tbody> </table>		 Pt	 $\text{Si}_3\text{N}_4$	 $\text{Pt}_x\text{Si}_y$	 Al	 Poly Si	 $\text{SiO}_2$	 Pyrex	
 Pt	 $\text{Si}_3\text{N}_4$	 $\text{Pt}_x\text{Si}_y$	 Al						
 Poly Si	 $\text{SiO}_2$	 Pyrex							



**Figure B.1:** SEM pictures of the fabricated conductive probe: a) the arrow points at the cantilever; b) V-shaped c) single-leg cantilevers; d) replicated mold shape from the backside of the cantilever; e) Tip array on the contact pad; f) tip on the cantilever.



**Figure B.2:** SEM pictures of the tip: a) whole tip with a base width of 5  $\mu\text{m}$ ; b) zoom-in on the freestanding metal tip with a base width of 80 nm; c) High magnification on the apex with a tip radius of 7nm.



**Part IV**

**Addendum**





# Acknowledgements

Of course it would not have been possible to accomplish all that work without the help of several people. At this point I would like to acknowledge all the people who contributed to the my thesis in a way or the other. I am grateful to Prof. N. de Rooij who gave me the chance to join his group. I am particularly grateful to my advisor and mentor Prof. U. Stauer for his time, his advises and wired ideas, for giving me inspiration and motivation on days where the sun didn't want to show up and for his skill to diplomatically solve non scientific issues encountered during my time in Neuchâtel. A special acknowledgment also goes to T. Akiyama for his guidance, help and great patience. A significant contribution to this work has been given by P. Frederix from the university of Basel, thank you for the endless discussions, the excellent advises and unlimited patience. I'm also grateful to Prof. A. Engel for introducing me to the fascinating world of structural biology. Many thanks to all the members of the 2002-2006 Nanotools group for the fruitful discussions at the Monday morning meetings. The Pontresina meeting will always stay in my mind. I would also like to thank Milena Koudelka-Hep for her introduction into SECM and her great advise and expertise in this domain. This was really the key point of success. I am grateful to the whole SAMLAB team of S. Jeanneret, E. Millotte, G. Mondin, N. Hegelbach, S. Pochon, J. Vaquera, S. Ischer and P.-A. Clerc, for their excellent and substations contribution to the fabrication of the devices. I also want to thank all the members of SAMLAB I did not mention personally for the pleasant time spent together. Last but not least I would like to acknowledge the SNF NCCR Nano scale science for the financial support.



# Publications

## B.1 Papers

Title: Towards a planar sample support for in situ experiments in structural biology

Authors: M. R. Gullo, T. Akiyama, P.L.T.M. Frederix, A. Tonin, U. Staufer, A. Engel, N.F. de Rooij

Journal: Microelectronic Engineering

Volume: 78-79

Pages: 571-574

Publisher: Elsevier

Title: Insulated conductive probes for in situ experiments in structural biology

Authors: M. R. Gullo, T. Akiyama, P.L.T.M. Frederix, A. Tonin, U. Staufer, A. Engel, N.F. de Rooij

Book: STM, ISBN 0-7354-0168-3

Pages: 166-171

Publisher: American Institute of Physics

Title: Assessment of insulated conductive cantilevers for biology and electrochemistry

Authors: P. Frederix, M. Gullo, T. Akiyama, A. Tonin, N.F. de Rooij, U. Staufer, A. Engel

Journal: Nanotechnology

Volume: 16

Pages: 997-1005

Publisher: Institute of Physics Publishing

Title: Development of Insulated Conductive Probes with Platinum Silicide Tips for Atomic Force Microscopy in Cell Biology

Authors: T. Akiyama, M. Gullo, N.F. de Rooij, A. Tonin, H.-R. Hidber, P. Frederix, A. Engel, U. Staufer

Journal: Japanese Journal of Applied Physics

Volume: 43

Pages: 3865-3867

Publisher: Japanese Journal of Applied Physics

Title: Characterization of Batch Fabricated Probes for Combined Atomic Force and High Resolution Scanning Electrochemical Microscopy

Authors: M. R. Gullo, T. Akiyama, P.L.T.M. Frederix, A. Tonin, U. Staufer, A. Engel, N.F. de Rooij

Journal: Analytical chemistry

Volume: 78 Pages: 5436-5442

Publisher: American chemical society

## **B.2 Proceedings**

### **B.2.1 Academic Year: 2004 – 2005**

Conference: Seeing at the nanoscale 2 (VEECO)

Place: Grenoble - France

Title: Planar sample support for in situ Experiments in Structural Biology

Authors: M. Gullo, T. Akiyama, N.F. de Rooij, P. Frederix, A. Engel, A. Tonin, U. Staufer

### **B.2.2 Academic Year: 2003 – 2004**

Conference: Micro and Nanoengineering MNE 2004

Place: Rotterdam - The Netherlands

Title: Planar sample support for in situ Experiments in Structural Biology

Authors: M. Gullo, T. Akiyama, N.F. de Rooij, P. Frederix, A. Engel, A. Tonin, U. Staufer

Conference: Scanning Probe Microscopies and Organic Materials

Place: Bielefeld - Germany

Title: Planar sample support for in situ Experiments in Structural Biology

Authors: M. Gullo, T. Akiyama, N.F. de Rooij, P. Frederix, A. Engel, A. Tonin, U. Staufer

Conference: Swiss Physical Society Annual Meeting SPS04

Place: Neuchatel - Switzerland

Title: Nanotools for Biology

Authors: M. Gullo, T. Akiyama, N.F. de Rooij, P. Frederix, A. Engel, A. Tonin, U. Staufer

Conference: 4eme Colloque Franco-Suisse

Place: Le Locle - Switzerland

Title: Sample preparation by means of electron beam lithography

Authors: U. Staufer, P.-A. Kunzi, S. Gautsch, L. Aeschimann, M. Gullo, N.F. de Rooij

Conference: LEA microtechnique Summer School "Highlights in Microtechnology"

Place: Neuchatel - Switzerland

Title: Fabrication of conductive AFM probes and sample supports for studying membrane proteins in a liquid environment

Authors: T. Akiyama, M. Gullo, P. Frederix, A. Engel, U. Staufer

### **B.2.3 Academic Year: 2002 – 2003**

Conference: 2th International Conference on STM and Related Techniques

Place: Eindhoven - The Netherlands

Title: Insulated Conductive Probes for in situ Experiments in Structural Biology

Authors: M. Gullo, T. Akiyama, P. Frederix, A. Engel, U. Staufer, N.F. de Rooij

Conference: SNF Review Pannel

Place: Basel - Switzerland

Title: Insulated Conductive Probes for in situ Experiments in Structural Biology

Authors: M. Gullo, T. Akiyama, N.F. de Rooij, P. Frederix, A. Engel, A. Tonin, U. Staufer

Conference: Twannberg Workshop on Nanoscience

Place: Twannberg - Switzerland

Title: Insulated Conductive Probes for in situ Experiments in Structural Biology

Authors: M. Gullo, T. Akiyama, N.F. de Rooij, P. Frederix, A. Engel, A. Tonin, U. Staufer

Conference: SPIE The International Society of Optical Engineering

Place: Maspaolomas, Gran Canaria - Spain

Title: Fabrication of Nano Interdigitated Electrodes

Authors: L. Berdondini, M. Kalbac, S. Gautsch, M. Gullo, U. Staufer, M. Koudelka-Hep, N.F. de Rooij

Conference: Annual Review Meeting of the National Center of Competence (NCCR) in Nanoscale Science

Place: Basel - Switzerland

Title: Highlights in Nanotools

Authors: U. Staufer, N.F. de Rooij, T. Akiyama, M. Gullo, R. Imer, K. Suter, P. Frederix, A. Engel, A. Tonin, M. Stolz, U. Aebi, K. Ensslin, A. Baumgartner